

Accurate Planetary Limb Localization for Image-Based Spacecraft Navigation

John A. Christian*

West Virginia University, Morgantown, West Virginia 26506

DOI: 10.2514/1.A33692

The use of images for spacecraft navigation is well established. Although these images have traditionally been processed by a human analyst on Earth, a variety of recent advancements have led to an increased interest in autonomous imaged-based spacecraft navigation. This work presents a comprehensive treatment of the techniques required to navigate using the lit limb of an ellipsoidal body (usually a planet or moon) in an image. New observations are made regarding the effect of surface albedo and terrain on navigation performance. Furthermore, study of this problem led to a new subpixel edge localization algorithm using Zernike moments, which is found to outperform existing methods for accurately finding the horizon's location in an image. The new limb localization technique is discussed in detail, along with extensive comparisons with alternative approaches. Theoretical results are validated through a variety of numerical examples.

I. Introduction

IMAGES of planets and moons have been used for spacecraft navigation in deep space for over 50 years [1]. This task, referred to as optical navigation (OPNAV) in the space navigation community, has traditionally been performed by human analysts on Earth. In a typical scenario, images are downlinked from the spacecraft; an analyst applies various image processing tools to precisely localize the observed celestial object(s) in each image [2]; these OPNAV observables are combined with radiometric tracking data in a batch filter to estimate the spacecraft state [3]; and the resulting navigation solution is then uplinked to the spacecraft.

Although this traditional approach remains popular today (because it is well understood and relatively low risk), advancements in onboard computing resources, image processing algorithms, and estimation techniques allow for the OPNAV portion of this process to be automated and performed entirely on the spacecraft. Thus, OPNAV has the potential to enable completely autonomous spacecraft navigation in the vicinity of a planet or moon.

There are two primary classes of OPNAV techniques for images of resolved celestial bodies: those using landmarks on the observed body's surface and those using the lit horizon. Landmark techniques tend to produce more accurate navigation results but are restricted to relatively close distances (where landmarks are large enough to be visible in imagery) and can be rather complicated to implement. Horizon-based techniques are usually less accurate than landmark methods but tend to remain viable at large distances from the observed body. Horizon-based techniques can also be implemented without a detailed terrain model, albedo map, or sophisticated scene rendering software, which often makes them simpler, faster, and more robust than landmark methods. Both of these approaches have found widespread use for OPNAV on past space exploration missions [2,4–8]. This work focuses only on horizon-based methods.

Additionally, as is discussed at length within this paper, atmospheres have historically posed a significant obstacle for OPNAV. Consequently, the focus of this paper will primarily be on atmosphereless bodies.

This paper provides a comprehensive and detailed discussion of the physics and mathematics of image-based spacecraft navigation using an ellipsoidal body's lit limb. Such ellipsoidal bodies are typically planets or moons, but the approach presented here may be applied to nearly any ellipsoidal body. In particular, this paper reviews the state of the art, corrects a variety of popular misconceptions, and introduces improved algorithms for many key aspects of this problem.

A. Background

Horizon-based navigation dates back to antiquity. Ancient mariners and explorers used the apparent elevation of stars above the horizon to maintain a constant latitude on their voyages [9] (the longitude problem proved to be much harder for early explorers [10]). This same idea was first applied to spacecraft navigation during NASA's Gemini Program, when astronauts tested a handheld space sextant to measure the angle between the apparent horizon and known reference stars [11–13]. This was a pathfinder experiment for the Apollo space sextant [14], which was used by the crew of Apollo 8 to demonstrate that star-horizon measurements could enable completely autonomous spacecraft navigation in cislunar space [15]. Space sextant experiments were also performed during the Skylab Program [16,17].

A crew-operated space stadimeter was also developed (but not flown) as part of the Gemini Program [12] and eventually demonstrated during the Skylab Program [16,17]. This optical device allowed a crewmember to manually measure the apparent angular diameter of the Earth from three limb sightings, providing information that could then be used to determine the vehicle's altitude (or, equivalently, the vehicle's distance from the center of the planet).

Crew-based OPNAV was largely abandoned with the beginning of the Space Shuttle era in the 1980s because such a capability is not needed for missions constrained entirely to low Earth orbit (LEO). Recently, however, there have been a few new crew-aided OPNAV concepts due to the return of interest in human exploration beyond LEO generated by NASA's Orion Program [18,19].

The same type of measurements that were taken manually by astronauts in these early experiments may also be extracted from an image. As a result, image-based OPNAV has become the norm for robotic space exploration missions [1,2]. Although OPNAV using images was first demonstrated on the Mariner 6 and 7 missions to Mars [1,20], the technique was found to be essential for missions to the outer planets (e.g., Voyager [5,21,22], Cassini [7], and New Horizons [8]).

Modern missions use a technique known as limb scanning to perform horizon localization of resolved bodies. This procedure was first used during the Voyager mission [21] and is described in detail in [2]. In brief, limb scanning works by taking an assumed body center and then generating a handful of scan directions emanating from this center point. The length of the scans are based on the body's apparent

Received 30 June 2016; revision received 26 December 2016; accepted for publication 22 January 2017; published online 12 April 2017. Copyright © 2016 by John A. Christian. Published by the American Institute of Aeronautics and Astronautics, Inc., with permission. All requests for copying and permission to reprint should be submitted to CCC at www.copyright.com; employ the ISSN 0022-4650 (print) or 1533-6794 (online) to initiate your request. See also AIAA Rights and Permissions www.aiaa.org/randp.

*Assistant Professor, Department of Mechanical and Aerospace Engineering, Benjamin M. Statler College of Engineering and Mineral Resources. Senior Member AIAA.

size in the image. Each scan generates a one-dimensional (1-D) intensity profile. The observed intensity profile along each scan direction is compared to an expected intensity profile based on an assumed relative state and body model, and the relative state is then iteratively updated to find the best agreement between the observed and predicted intensity scans.

The work described in this paper takes a fundamentally different approach. Instead of using limb scans, an approach based on whole limb fitting is pursued. Although the foundations for whole limb fitting were put forward in [23,24], this early work was quite primitive. The idea has since been substantially improved upon by a variety of different researchers [25–33]. The present work provides a significant improvement to this existing body of literature by providing a detailed look at accurate limb localization rooted in OPNAV geometry, planetary photometry, and limb modeling.

B. The Case for Limb-Only OPNAV

Suppose that a vehicle is far enough away from a body that limb-based measurements are more desirable than landmark measurements (or that operational constraints preclude landmark methods). Under such a scenario, two variations of horizon-based OPNAV exist: limb–star OPNAV and limb-only OPNAV.

Limb–star OPNAV closely parallels the measurement type produced by space sextant measurements and is also commonly used for image-based OPNAV. Processing stars that appear in the same image as a resolved body help produce a better estimate of the camera's pointing direction and, therefore, a better estimate of the spacecraft's inertial position relative to the body. There are, however, two main difficulties with limb–star measurements.

The first difficulty is that stars appear much dimmer than planets or moons (this is especially true for the Earth and Moon). This fact, coupled with limitations on the dynamic range of modern imagers, makes it difficult to properly expose both stars and planets in the same image. The usual solution is to collect three images in rapid succession (a short-exposure image for the planet sandwiched between two long-exposure images for the stars). The camera's attitude during the short-exposure image is estimated by interpolating between the attitudes found using the stars in the two long-exposure images. This approach, however, introduces its own set of difficulties associated with 1) obtaining three sequential images of proper exposure and quality, 2) nonconstant vehicle rotation that may occur between the three images, and 3) obtaining sufficiently accurate image time stamps.

The second difficulty with limb–star measurements is the availability of star sightings in scenarios where OPNAV is most important. One of the primary motivations for the contemporary study of OPNAV is to provide a backup to ground-based radiometric tracking. If such a navigation backup is being exercised, then some other significant failure has already occurred. In light of this, the Apollo 13 mission provides an illustrative example [34]. During Apollo 13, the explosive failure of the service module #2 oxygen tank created a debris field around the spacecraft. This debris field made it impossible for the astronauts to take star sightings, as they were unable to distinguish between stars and debris. An automated system is likely to encounter similar problems in positively identifying stars for limb–star measurements with a sufficiently high degree of confidence.

Therefore, the capability to perform limb-only OPNAV is important. More specifically, the aim is to estimate the relative position between the spacecraft and the observed celestial body in the camera frame using only the body's lit limb. To arrive at the relative position in the inertial frame requires attitude information from another source. Additionally, if usable stars do appear in an OPNAV image, they may be processed separately to better align the camera frame with the inertial frame at the time the image was taken.

C. Contribution and Paper Organization

This paper provides a comprehensive treatment of the image processing and estimation required to perform horizon-based OPNAV. In doing so, this paper offers significant improvements to the current state of the art and corrects many misconceptions being perpetuated in the contemporary literature. Although this necessitates

a review of some known topics, important and novel insights are made throughout. Therefore, the paper is organized as follows.

First, a review of the geometry of the OPNAV problem and the associated estimation of spacecraft position from observed horizon points is presented. The method used here provides an exact and noniterative solution for observations of a smooth ellipsoidal body (which, again, is usually a planet or moon). The relations described in this section form the foundation upon which everything else is built.

Second, a detailed analysis of the limb's appearance in an image is presented, with discussion of atmospheric effects, reflectance models, and local terrain. Of particular note are new observations on how both albedo and terrain can influence the quality of the final OPNAV measurements.

Third, a complete methodology for accurate limb finding is presented. The study of this problem led to the development of a novel subpixel edge localization technique based on Zernike moments. A comparison is made with 11 other edge localization techniques, and the new approach is found to exhibit substantially better performance.

Fourth, a variety of observations are made through the use of numerical results. It is shown that sophisticated iterative model fitting approaches provide no performance improvement to the noniterative technique presented in the preceding sections of this paper. It is also shown that terrain is often the dominant error source in the final OPNAV solution. Additionally, examples of edge localization performance and OPNAV performance are provided.

II. Geometry and Solution Method for Horizon-Based Optical Navigation

A. Horizon-Based Optical Navigation Is a Conic Section Problem

The horizon arc of a smooth ellipsoidal planet or moon will typically appear as an ellipse in an image. Other conic sections are possible (e.g., a hyperbolic horizon arc), but these are only encountered at low altitudes when horizon-based OPNAV is not viable for a variety of other reasons [28]. Some key results from the geometry of the perspective projection of an ellipsoidal body are now reviewed and will be used extensively throughout the discussions that follow.

The shape of many planets and moons of interest for OPNAV may be well approximated by a triaxial ellipsoid. Thus, the surface of such a body obeys the constraint

$$\mathbf{p}^T \mathbf{A} \mathbf{p} = 1 \quad (1)$$

where \mathbf{p} is a 3×1 vector describing a point on the body's surface with respect to the body's center, and \mathbf{A} is a 3×3 symmetric positive-definite matrix describing the shape of the body. Although the expression in Eq. (1) is true in any frame, all subsequent discussions will assume that quantities are expressed in the camera frame. As a result, the body shape matrix \mathbf{A} may be computed as [26,29]

$$\mathbf{A} = \mathbf{T}_C^P \begin{bmatrix} 1/a^2 & 0 & 0 \\ 0 & 1/b^2 & 0 \\ 0 & 0 & 1/c^2 \end{bmatrix} \mathbf{T}_P^C \quad (2)$$

where $\{a, b, c\}$ are the lengths of the body's principal axes, and \mathbf{T}_C^P is the rotation matrix from the celestial body's principal axis frame P to the camera frame C .

It is clear, therefore, that the orientation of the body's principal axis frame as seen from the spacecraft is necessary to construct \mathbf{A} for a nonspherical body, and such relative attitude information is almost always available in practice. The celestial body's orientation does not matter if the body is spherical.

Now, suppose that a spacecraft equipped with a calibrated camera [35] is located at position \mathbf{r} relative to the center of the observed celestial body. Further, suppose that this camera captures an image of the body, such as shown in Fig. 1. The rays emanating from the camera that trace the apparent horizon form a cone that tightly bounds the ellipsoidal body. This is shown graphically in Fig. 2. Thus, any point on the surface of this cone obeys the constraint [26]



Fig. 1 Example image of Earth's moon that might be used for OPNAV.

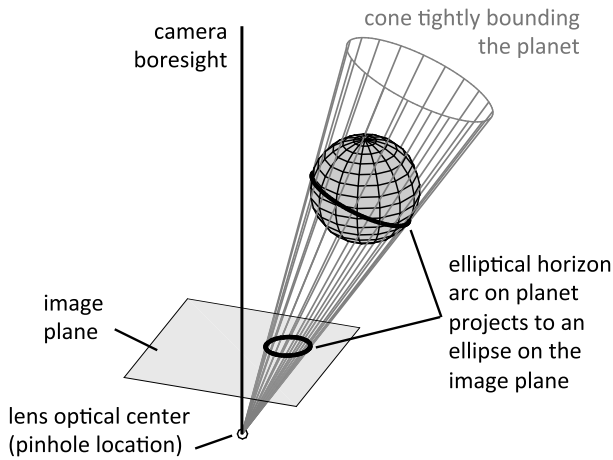


Fig. 2 Three-dimensional geometry of the perspective projection of a triaxial ellipsoid onto the image plane.

$$s_i^T M s_i = 0 \quad (3)$$

where s_i is a 3×1 vector describing a point on the cone, and M is a 3×3 symmetric matrix given by

$$M = A r r^T A - (r^T A r - 1) A \quad (4)$$

A detailed derivation and discussion of this expression for the tightly bounding cone, along with some of its important properties, may be found in [26]. It is also evident from Eq. (3) that $M s_i$ forms a vector perpendicular to the cone anywhere along the horizon ray described by s_i . Consequently, $M s_i$ also describes the body's surface normal direction at the horizon location corresponding to the ray s_i .

Assuming a pinhole camera model, the perspective projection of the apparent horizon onto an image is a conic section problem. The pinhole camera model is given by

$$x = f \frac{X}{Z} \quad y = f \frac{Y}{Z} \quad (5)$$

where f is the camera focal length, $\{X, Y, Z\}$ is the three-dimensional location of the observed point in the camera frame, and $\{x, y\}$ is the corresponding two-dimensional (2-D) coordinate in the image plane. The Z axis is along the camera boresight and is positive out of the camera. It is possible to set $f = 1$ and work in focal-length-normalized coordinates without loss of generality. Furthermore, it is convenient to work in the image plane (instead of the focal plane) to avoid dealing with a flipped image [36].

When working in focal-length-normalized coordinates, each horizon ray found in the image plane may be described by

$s_i = [x_i \ y_i \ 1]^T$. Substituting this into Eq. (3), it is clear that this is nothing more than taking a slice of the cone with the $Z = 1$ plane. This intersection is described by the implicit quadratic equation

$$m_{11}x_i^2 + 2m_{12}x_iy_i + 2m_{13}x_i + m_{22}y_i^2 + 2m_{23}y_i + m_{33} = 0 \quad (6)$$

where m_{jk} describes the $\{j, k\}$ element of the symmetric matrix M from Eq. (4). Thus, horizon-based OPNAV is a conic section problem. Furthermore, if the spacecraft position r and the body shape A are known, then the horizon ellipse in the image may be found analytically by computing M and evaluating Eq. (6). The detailed mathematics of horizon projections are discussed at length in [28] and are omitted here.

Before proceeding further, it is important to note that the center of the celestial body's elliptical projection in an image does not produce a line-of-sight direction pointing toward the center of the body. This fact has been known for some time, and various authors have presented corrections for this effect [23,32,33]. Although much has been written about this in the literature, it is straightforward to sidestep this problem entirely by intelligently constructing the estimation problem. Examples of approaches that solve the exact perspective projection of an ellipsoidal body onto an image without going through the intermediate (and unnecessary) step of computing the ellipse center include [26,28,29].

B. Solving for Spacecraft Position from Observed Limb Points

Suppose that a set of pixel coordinates corresponding to a body's lit limb, $\{u_i, v_i\}_{i=1}^m$, are available. It is straightforward to convert these pixel coordinates into image plane coordinates using the camera's intrinsic parameters. Because the pixel coordinates are related to the image plane coordinates by the well-known relation [36]

$$\begin{bmatrix} u_i \\ v_i \\ 1 \end{bmatrix} = \begin{bmatrix} d_x & \alpha & u_p \\ 0 & d_y & v_p \\ 0 & 0 & 1 \end{bmatrix} \begin{bmatrix} x_i \\ y_i \\ 1 \end{bmatrix} \quad (7)$$

it is possible to analytically invert this expression to find the desired relation

$$s_i = \begin{bmatrix} x_i \\ y_i \\ 1 \end{bmatrix} = \begin{bmatrix} \frac{1}{d_x} & \frac{-\alpha}{d_x d_y} & \frac{\alpha v_p - d_y u_p}{d_x d_y} \\ 0 & \frac{1}{d_y} & -\frac{v_p}{d_y} \\ 0 & 0 & 1 \end{bmatrix} \begin{bmatrix} u_i \\ v_i \\ 1 \end{bmatrix} \quad (8)$$

where d_x is the ratio of focal length to pixel pitch in the x direction (and d_y is the same thing in the y direction), α is the detector array skewness, and $[u_p, v_p]$ is the principal point (where the boresight pierces the image plane). The pixels are square if $d_x = d_y$, and the detector's pixel columns are orthogonal to the pixel rows if $\alpha = 0$. Note that this transformation between image plane coordinates (x and y) and image pixel coordinates (u and v) assumes the standard frame convention as shown in Fig. 3. This convention places the origin of the u - v frame in the upper left-hand corner of the image, with positive u to the right in the image (corresponding to image columns) and positive v down in the image (corresponding to image rows). The diagram in Fig. 3 is drawn from the vantage point of the lens optical center (i.e., looking out of the camera with the positive Z direction into the page).

The best known solution for finding the spacecraft's planet relative position r from a set of observed horizon points in the image plane, $\{s_i\}_{i=1}^m$, makes use of matrix factorization to solve the problem exactly and without iteration. The result, which may be implemented in only a few lines of code, is an estimate of the spacecraft (or camera) position that produces the projected horizon arc that best fits the noisy horizon measurements. The algorithmic solution is presented here without proof, and the interested reader is directed to [29] for details.

Begin by factoring the body's shape matrix into the form

$$A = B^T B \quad (9)$$

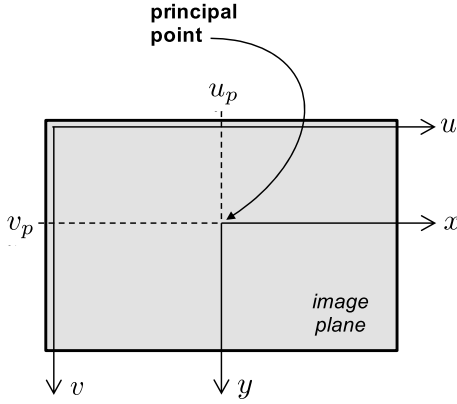


Fig. 3 Graphical depiction of image coordinate systems with $\alpha = 0$.

Such a form is guaranteed to exist because the matrix A is both symmetric and positive-definite. There are multiple valid factorizations that satisfy Eq. (9), but the specific choice of factorization is not important at this point in the discussion.

Now, use the factored matrix B to transform s_i [which is obtained from the measured horizon points via Eq. (8)] into a new “factorized space”:

$$\bar{s}_i = B s_i \quad (10)$$

and then unitize the transformed horizon observations:

$$\bar{s}'_i = \bar{s}_i / \|\bar{s}_i\| \quad (11)$$

For the interested reader, the geometric meaning of this transformation is discussed at length in [29].

From here, the solution is a simple linear least-squares problem. After finding the least-squares solution for the 3×1 vector n to the following overdetermined linear system:

$$\begin{bmatrix} \bar{s}'_1{}^T \\ \bar{s}'_2{}^T \\ \vdots \\ \bar{s}'_m{}^T \end{bmatrix} n = \mathbf{1}_{m \times 1} \quad (12)$$

the optimal estimate for the camera location \hat{r} is simply the solution to

$$B\hat{r} = -(n^T n - 1)^{-(1/2)} n \quad (13)$$

The matrix B is guaranteed to be both invertible and well conditioned for all reasonable celestial bodies, and so the solution for \hat{r} may also be written more directly as

$$\hat{r} = -(n^T n - 1)^{-(1/2)} B^{-1} n \quad (14)$$

This solution is strikingly simple, especially considering that the result is exact, and the only assumptions made are 1) that the planet or moon is a smooth triaxial ellipsoid, and 2) that the image is formed by perfect perspective projection (the pinhole camera model).

The ease by which Eq. (13) may be solved for \hat{r} depends on the choice of factorization to construct B in Eq. (9). Two such factorizations produce especially useful results: Cholesky decomposition and singular value decomposition (SVD). Importantly, both the Cholesky and SVD methods permit a solution without requiring a matrix inverse, which is desirable for many spaceflight applications. The naive approach of left multiplying Eq. (13) by B^{-1} [which leads to Eq. (14)] also works when computing matrix inverses are permitted. The results for the Cholesky and SVD methods are now briefly summarized.

1. Solution by Cholesky Decomposition

Suppose that the body’s shape matrix is factorized by a Cholesky decomposition. Efficient and numerically stable implementations of the Cholesky factorization are available in most linear algebra software packages and have been used in past spaceflight missions. In this case, let $B = U$, where U is an upper triangular matrix. Therefore,

$$A = B^T B = U^T U \quad (15)$$

Such a factorization is guaranteed to both exist and be unique for this case because A is a real valued, symmetric, positive-definite matrix [37]. Because $B = U$ is upper triangular, Eq. (13) may be efficiently solved without matrix inversion through backward substitution.

2. Solution by Singular Value Decomposition

Although prior work on this method focused on the Cholesky decomposition [29], the SVD produces an even simpler solution for \hat{r} in Eq. (13). Note that, although the SVD is used in the derivation, the SVD of A need not actually be computed to arrive at the solution.

Therefore, suppose that the body’s shape matrix is factorized by the SVD,

$$A = U S V^T \quad (16)$$

where U and V are orthogonal matrices, and S is a diagonal matrix of singular values (note that the matrix U here is different from that of the Cholesky factorization) [37]. Because A is real valued, symmetric, and positive-definite, $U = V$, and all the diagonals of S are greater than zero. Indeed, the SVD of the matrix A is nothing more than the expression from Eq. (2), which leads to

$$U = V = T_C^P \quad \text{and} \quad U^T = V^T = T_C^C \quad (17)$$

and

$$S = \begin{bmatrix} 1/a^2 & 0 & 0 \\ 0 & 1/b^2 & 0 \\ 0 & 0 & 1/c^2 \end{bmatrix} \quad (18)$$

Recall that the values $\{a, b, c\}$ are the dimensions of the principal axes of the ellipsoidal body, and therefore, the diagonal elements in S are all strictly greater than zero. It is now trivial to factorize the matrix S as

$$S = Q^T Q \quad (19)$$

where

$$Q = \begin{bmatrix} 1/a & 0 & 0 \\ 0 & 1/b & 0 \\ 0 & 0 & 1/c \end{bmatrix} \quad \text{and} \quad Q^{-1} = \begin{bmatrix} a & 0 & 0 \\ 0 & b & 0 \\ 0 & 0 & c \end{bmatrix} \quad (20)$$

Therefore, substituting these results into Eqs. (9) and (16),

$$A = B^T B = (T_C^C)^T Q^T Q T_C^C \quad (21)$$

which leads directly to

$$B = Q T_C^P \quad (22)$$

Importantly, the matrix B has an analytic inverse because T_C^P is an orthogonal matrix (a direction cosine matrix), and Q^{-1} is given by Eq. (20). That is,

$$B^{-1} = (Q T_C^P)^{-1} = (T_C^P)^{-1} Q^{-1} = (T_C^P)^T Q^{-1} = T_C^C Q^{-1} \quad (23)$$

Therefore, after substitution of this result into Eq. (14), one arrives at

$$\hat{r} = -(n^T n - 1)^{-(1/2)} T_C^P Q^{-1} n \quad (24)$$

where \mathbf{n} is from Eq. (12), T_C^P is the known rotation from the body principal axis frame to the camera frame, and \mathbf{Q}^{-1} is a diagonal matrix of the body's principal axis dimensions as given in Eq. (20). Note that this solution for $\hat{\mathbf{r}}$ does not require the numeric inversion of a matrix, nor does it require that any matrix factorization actually be performed.

III. Properties of a Lit Planetary Limb as Viewed from a Camera in Space

The planets and moons in our Solar System are naturally illuminated by the sun. Consequently, the apparent brightness and photometric behavior of a particular celestial body in a digital image is governed by how its surface (and/or atmosphere) scatters light. The subsections that follow discuss the challenges with atmospheres, reflectance models for celestial bodies, and local terrain.

A. Atmospheres Complicate Limb Localization

Gaseous planetary atmospheres scatter incident sunlight through a variety of processes [38,39]. Observations of Earth's atmosphere from space, for example, are dominated by Rayleigh scattering [40] and Mie scattering [41]. Over the last 20 years, there has been a great deal of work on the rapid evaluation of such scattering to accurately render an atmosphere's appearance in an image [42–44]. Although the synthetic images produced by these rendering techniques may look realistic, they are not necessarily predictive.

Some authors have suggested that planetary atmospheres soften (or smooth out) the apparent horizon and, therefore, improve the accuracy of limb localization and the resulting OPNAV state estimate [32]. We, however, argue the opposite for two important reasons. First, the atmosphere does not soften the horizon edge, but obscures it, creating a new apparent horizon at some altitude above the actual planetary surface. Second, the altitude of this new apparent horizon is difficult to accurately predict because it is a function of weather, complicated scattering of sunlight in a heterogeneous atmosphere, and the illumination/viewing geometry.

It has long been known that the apparent horizon for a body with an atmosphere occurs at some altitude above the planet's surface. For example, this was a major challenge for Earth limb-star measurements with the space sextant during the Apollo Program, where each astronaut had a personalized "calibration" for the spot in the atmosphere they would mark as the horizon [15]. Others have done something similar with imagery by inflating the planet's size with an atmospheric altitude parameter [23,32]. The challenge, again, is that this apparent altitude is highly variable and difficult to predict.

For these reasons, the discussions that follow will focus primarily on bodies with no atmosphere (e.g., Moon, Mercury). Such bodies have a crisp horizon along the lit limb, with an intensity gradient across the horizon driven largely by the camera's point spread function (PSF). The decision to focus on atmosphereless bodies is consistent with past operational experience on actual spacecraft missions. To date, most robotic planetary exploration missions have avoided performing OPNAV with bodies having an atmosphere (e.g., Venus, Earth, Titan, any of the gas giants) for four primary reasons. First, the accuracy of atmospheric models is difficult to verify ahead of time. Second, atmospheric models of sufficient fidelity tend to be very complicated and difficult to implement (by an analyst on Earth) within the demanding and fast-paced context of ground operations. Third, the temporal variability of atmospheres can be significant and often makes steady-state atmosphere models ineffectual for precision OPNAV applications. A classic example is cloud formations, which are hard to model, can change significantly over a short period of time, and often have a dominant effect on the appearance of an object in an image (see [24] for an example with clouds on Earth). Fourth, it has been possible (thus far) to successfully navigate all missions using only radiometric navigation and optical observations of objects with no atmosphere, thus making it unnecessary to invest the substantial resources required to adequately mature techniques for dealing with an atmosphere.

In summary, accurate horizon-based OPNAV using bodies with an atmosphere is challenging and is a topic of ongoing research. The interested reader is directed to [45] for more details.

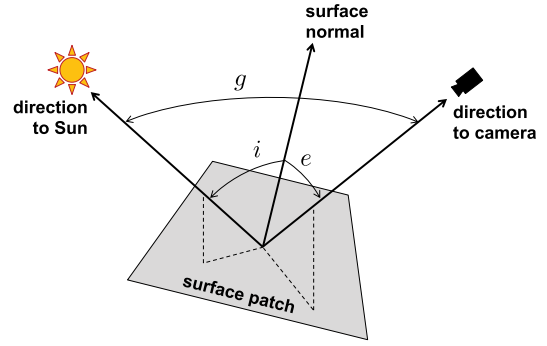


Fig. 4 Depiction of angles defining the BRDF.

B. Reflectance Models for Atmosphereless Bodies

The reflectance of a planetary surface is described by its bidirectional reflectance distribution function (BRDF). A BRDF defines the ratio of the reflected radiance to the incident irradiance and is generally a function of the surface properties, the wavelength of light, and the viewing/lighting geometry. The viewing/lighting geometry is generally parameterized by three angles: incidence angle i , emission angle e , and phase angle g . These angles are shown in Fig. 4.

1. Simple Reflectance Models

The simplest reasonable reflectance model follows the empirically derived Lambert's law (ideal diffuse reflection), where the radiance is the same in all directions. For a Lambertian surface, the reflectance is only a function of the Lambert albedo A_L and the incidence angle i :

$$r_L(i, e, g) = \frac{A_L}{\pi} \cos i \quad (25)$$

Lambert's law, first published in the mid-1700s [46], has been an enduring photometric relationship due to its simplicity and wide applicability for high-albedo surfaces (which are commonly encountered in everyday life on Earth). Most planetary bodies, however, have a low albedo and are not well modeled as Lambertian objects.

The Lommel–Seeliger law is a slightly more sophisticated model, which considers both the incidence and emission angles [47–50]. First posited in the late 1800s (see Appendix A), it is the simplest model that may be derived directly from the radiative transfer equation [51–53] and is given by

$$r_{LS}(i, e, g) = \frac{w}{4\pi} \frac{\cos i}{\cos i + \cos e} \quad (26)$$

where w is the single scattering albedo. Despite its limitations, this model has found widespread use in planetary photometry. Of particular note is that the Lommel–Seeliger law assumes a smooth surface and, therefore, predicts a surge in apparent brightness near the limb (an effect known as limb brightening). Natural bodies with a reasonable degree of macroscopic surface roughness, such as the Moon, do not exhibit such limb brightening. This shortcoming of the Lommel–Seeliger law in accurately predicting limb brightness is especially important in the present context, where the focus is on navigation using the body's lit limb.

Thus, a more sophisticated model is needed. Two such models are now considered: the Kasseleinen–Shkuratov model and the Hapke model.

2. Kasseleinen–Shkuratov Model

The Kasseleinen–Shkuratov (KS) model [54,55] is an empirical model that has become quite popular in recent years for modeling the surface scattering of atmosphereless bodies, including the Moon [55], Mercury [56], and Vesta [57]. The KS model has a rather simple functional form of

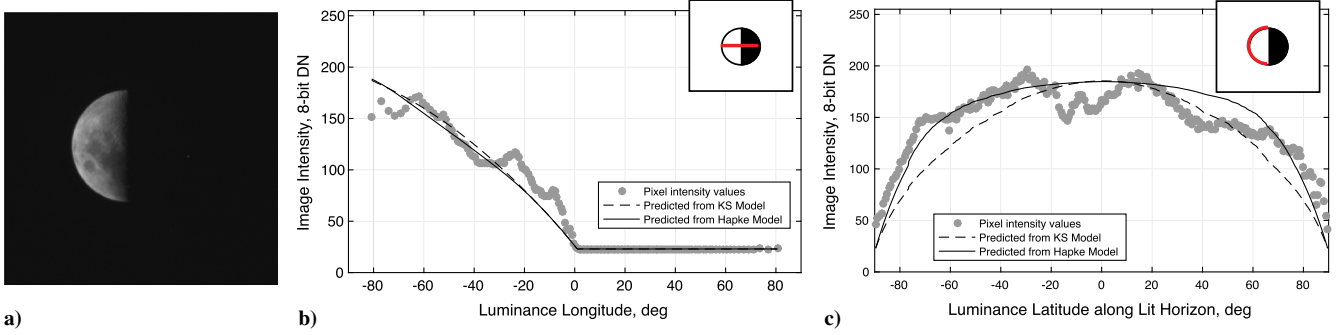


Fig. 5 Comparison of analytic reflectance models to flight data for the moon: a) real image of the Moon from Cassini (raw image is W1313634451_1.IMG [68]), b) comparison along the luminance equator, and c) comparison along the lit limb.

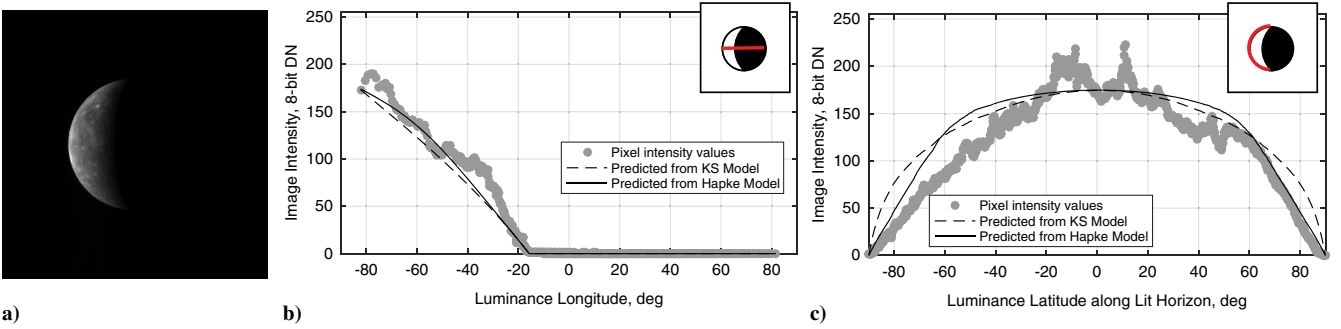


Fig. 6 Comparison of analytic reflectance models to flight data for Mercury: a) real image of Mercury from MESSENGER (raw image is EN0162637138M.IMG [69]), b) comparison along the luminance equator, and c) comparison along the lit limb.

$$r_{KS}(i, e, g) = \frac{A_{eq}(\lambda, g)}{\pi} D(i, e, g, \lambda) \quad (27)$$

where λ is the wavelength of light, $A_{eq}(\lambda, g)$ is the albedo, and $D(i, e, g, \lambda)$ is the disk function. Although a variety of disk functions have been presented, the one yielding the best agreement with empirical observations is simply a single parameter c_l blending of the Lambert and Lommel–Seeliger scattering laws:

$$D(i, e, g, \lambda) = c_l \frac{2 \cos i}{\cos i + \cos e} + (1 - c_l) \cos i \quad (28)$$

This rather popular disk model has a long history that predates the KS model itself and has been used by a wide variety of authors for a wide variety of celestial bodies over the past 30 years [55–60].

3. Hapke Model

Consider the complete Hapke model, which was incrementally developed by Bruce Hapke over a 30 year period [52,61–65] and is concisely summarized in Sec. 12.3.1 of [66]. This model has seen widespread use in both the planetary photometry and computer vision communities because of its theoretically rigorous underpinnings, eloquent presentation, and generally accurate prediction of empirical observations. Thus, using the complete model from [66],

$$r_H(i, e, g) = K \frac{w}{4\pi} \left(\frac{\cos i_e}{\cos i_e + \cos e_e} \right) \left\{ P(g) [1 + B_{S0} B_S] + \left[H \left(\frac{\cos i_e}{K} \right) H \left(\frac{\cos e_e}{K} \right) - 1 \right] [1 + B_{C0} B_C(g)] S(i, e, g, \bar{\theta}) \right\} \quad (29)$$

where i_e and e_e are the effective incidence and emission angles; K is a porosity term; $P(g)$ is the single-particle scattering function; B_{S0} and B_S describe the shadow-hiding opposition effect; B_{C0} and B_C model describe the coherent backscatter opposition effect; and $S(i, e, g, \bar{\theta})$ describes the macroscopic roughness (parameterized by the mean

slope angle $\bar{\theta}$). The reader is directed to [66] for the full expressions for each of these terms because they are too long to present within the length constraints of this paper.

The parameters for the complete Hapke model have been estimated for a variety of celestial bodies, including the Moon [67] and Mercury [56].

4. Comparison of Reflectance Models

Although the KS model is much simpler, the Hapke model is found to provide a better fit to the observed data along the lit limb, at least for the Moon (see Fig. 5 [68]) and for Mercury (see Fig. 6 [69]). The image of the Moon is from the Cassini wide-angle camera and was taken during the spacecraft's August 1999 flyby of Earth (the raw image data have been cropped around the Moon to make it more visible in this figure). The image of Mercury is from the MESSENGER narrow-angle camera and was taken during the spacecraft's September 2009 flyby of Mercury. The data for both the Cassini and MESSENGER images were obtained from the NASA Planetary Data System Cartography and Imaging Sciences Discipline Data[†] and were processed into a displayable format using the NASAView v3.13.0 software. Image intensity values are shown units of digital number (DN). As monochrome 8-bit images, these intensity values range from 0 (black) to 255 (white).

Note that the predicted intensity profiles for the KS and Hapke models in Figs. 5 and 6 assume an average global albedo. Much of the undulation of the real intensity values about the predicted intensity values is due to regional variations in albedo. Further, as is evident from the discussion in Sec. II.A and Fig. 3, observe that the horizon arc is not a great ellipse (or a great circle in the case of a spherical body). As a result, the lit limb profiles in Figs. 5c and 6c are not arcs of constant luminance longitude.

That the Hapke model outperforms the KS model along the limb makes intuitive sense because the empirical KS model does not account for the surface roughness effect that dominates along the

[†]Data available online at <http://pds-imaging.jpl.nasa.gov> [retrieved 15 April 2016].

horizon (especially along the horizon near the poles). This effect, however, is explicitly captured in the Hapke model. Furthermore, this apparent darkening of the limb near the luminance poles (also referred to as cusps) has significant practical implications for image-based OPNAV. As the poles darken, the quality of the horizon localization is substantially degraded. This is true for illuminated planetary disks of all phases, but is especially true for high phase angles (illuminated disks of crescent shape) where the terminator begins to encroach on the already darkened polar horizon.

The KS and Hapke models predict the apparent brightness at any point on the illuminated disk. Here, however, the focus is specifically on the 1-D intensity profiles along the lit limb. Although these models may be used with an average albedo to obtain the general intensity variations on a global level (as was done in Figs. 5 and 6), accurate modeling of the limb intensity profile requires an albedo map and knowledge of the specific portions of the body's surface being imaged. This modeling requirement is contrary to one of the primary advantages of horizon-based OPNAV, specifically, its ability to be used without requiring a detailed map of surface features, texture, and albedo. Fortunately, as will be seen in subsequent discussions, completely predicative limb modeling is not found to be necessary, and a different approach may be used.

C. Effect of Local Terrain

Although it is often convenient to assume that celestial bodies are smooth ellipsoids, this is only an approximation. Actual planets and moons with little or no atmosphere have a rough surface due to geological processes, impact events, and space weathering. Thus, local terrain is an important consideration and, in many cases, is found to be the limiting factor on end-to-end performance of horizon-based OPNAV.

A celestial body's terrain is typically captured in a digital elevation model (DEM), which describes the surface elevation above an equipotential reference ellipsoid. The construction of DEMs is a standard science data product for most space exploration missions, and high-quality DEMs are available for many bodies in our Solar System through NASA's Planetary Data System. Because the reference ellipsoid is typically used as the body shape within OPNAV algorithms, the DEM effectively describes the model error associated with the smooth ellipsoid approximation.

Table 1 lists the maximum elevation deviations from the reference ellipsoid for a few key bodies within our Solar System. Subpixel edge finding techniques, such as described in Sec. IV.D, are capable of detecting an edge location to better than 0.1 pixel. Therefore, assuming that the maximum elevation deviation represents a 3σ dispersion, it is possible to calculate the apparent radius where errors from terrain are statistically equivalent in magnitude to errors from edge finding (shown in the last column of Table 1 [70–72]). It is immediately evident that terrain will be an important factor in overall OPNAV performance for most images, which often contain apparent diameters of a few hundred pixels. An object will have larger relative terrain errors when it is nearby (larger apparent radius in image) and will have lower relative terrain errors when it is far away (smaller apparent radius in image). This is one of the reasons landmark tracking becomes superior at close distances.

The general guidelines from Table 1 may be replaced with a more sophisticated analysis when adequate data are available. As an illustrative example, consider Earth's moon using data from the Lunar Orbiter Laser Altimeter (LOLA) [73], which flew aboard NASA's Lunar Reconnaissance Orbiter mission [74]. A variety of DEMs have been created using LOLA data, and an example is shown

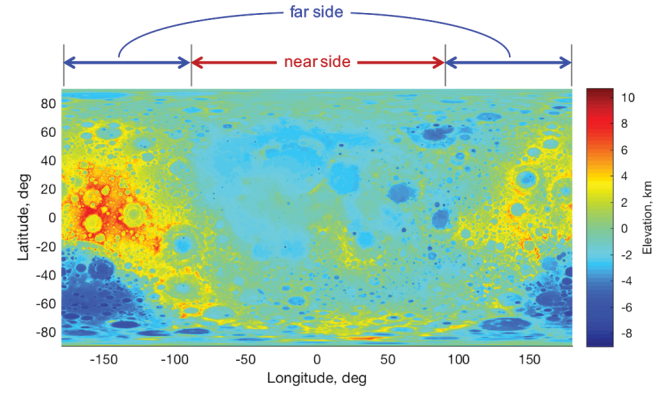


Fig. 7 Visualization of lunar DEM shows that the far side of the Moon exhibits more elevation variation than the near side.

in Fig. 7. This particular example was constructed by the author using the data from [75].

The Moon is tidally locked with the Earth, causing the same side of the Moon to always face the Earth (although librations cause the Moon to wobble slightly, allowing Earth-bound observers to view a little more than half the lunar surface over time). As a consequence, the far side of the Moon is not shielded by the Earth and has experienced significantly more impact events than the near side. This has led to very different topological profiles between the two lunar hemispheres (see Fig. 7) and requires that different terrain models be developed for the Moon's near side and far side.

Recall that one of the main objectives of horizon OPNAV is to enable vision-based navigation without the evaluation of a detailed body-fixed DEM. Therefore, it is proposed that the terrain be described by a statistical model that can be applied everywhere on the body without regard for the specific terrain features that may be affecting the horizon in any particular image.

Suppose that the elevation profile along an arc on a body's surface (e.g., the horizon arc) is given by $h(\theta)$ and is described by a first-order Gauss–Markov process:

$$\frac{\partial h(\theta)}{\partial \theta} = -\frac{1}{\tau} h(\theta) + \nu \quad (30)$$

where θ is the angle along the planetary arc, τ is the “time” constant, and ν is a zero-mean white noise process with intensity σ_ν . This stochastic differential equation can be solved exactly [76], allowing the construction of a discrete process that may be used if one wishes to simulate a particular random elevation profile:

$$h(\theta_{k+1}) = h(\theta_k) \exp\left[-\frac{\Delta\theta}{\tau}\right] + w_k \quad (31)$$

where $\Delta\theta = \theta_{k+1} - \theta_k$ is the step size used when “propagating” the elevation along the horizon arc, and w_k is a random number drawn at each step from a zero-mean Gaussian distribution with a variance of σ_w^2 :

$$\sigma_w^2 = \frac{\sigma_\nu^2 \tau}{2} \left\{ 1 - \exp\left[-2\frac{\Delta\theta}{\tau}\right] \right\} \quad (32)$$

An example is shown graphically in Fig. 8.

Now, it is possible to use the LOLA-generated DEM to estimate values for both τ and σ_ν for the Moon. To do this, recall that the Gauss–Markov process has a steady-state variance of

$$\sigma_{h,ss}^2 = \frac{\tau \sigma_\nu^2}{2} \quad (33)$$

which may be rearranged to find σ_ν :

$$\sigma_\nu = \sqrt{2} \frac{\sigma_{h,ss}}{\sqrt{\tau}} \quad (34)$$

Table 1 Maximum elevation deviations for a selection of bodies in our Solar system

Celestial body	Equatorial radius, km	Maximum elevation, km	Apparent radius where terrain becomes important, pixels
Mercury [70]	2439.8	4.02	182
Earth	6378.1	8.85	217
Moon [71]	1737.2	10.78	48
Mars [72]	3396.2	4.85	210

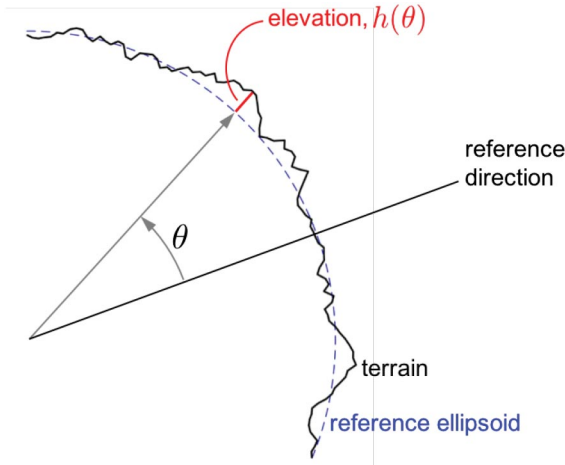


Fig. 8 The elevation of the terrain along any elliptical arc on the reference ellipsoid may be modeled as a first-order Gauss–Markov process.

Gauss–Markov processes also have an exponential autocorrelation function:

$$R_h(\delta\theta) = \sigma^2 \exp\left[-\frac{\delta\theta}{\|\tau\|}\right] \quad (35)$$

which may be used to find the time constant. This is done by simply finding the value of $\delta\theta$ that produces $R_h(\delta\theta)/\sigma^2 = \exp(-1) = 0.368$ from the autocorrelation plot generated by a particular elevation arc in the LOLA data.

As was mentioned briefly before, the statistics of the elevation variability are quite different between the near side and the far side, a fact that is qualitatively evident in Fig. 7 and quantitatively described in Fig. 9. Despite the separation of the near and far lunar hemispheres, there is still a considerable amount of variability from one horizon arc to another. For the near side, it is found that $\sigma_{h,ss} = 1.3 \pm 0.5$ km and $\tau = 10.0 \pm 8.8$ deg. Likewise, for the far side, it is found that $\sigma_{h,ss} = 2.8 \pm 1.5$ km and $\tau = 20.2 \pm 18.8$ deg. In both cases, the distributions of $\sigma_{h,ss}$ and τ appear to be relatively uniform across the given ranges. Thus, horizon arcs formed by the Moon’s near side are less noisy than horizon arcs formed by the far side, resulting in better performance when using near-side horizon arcs.

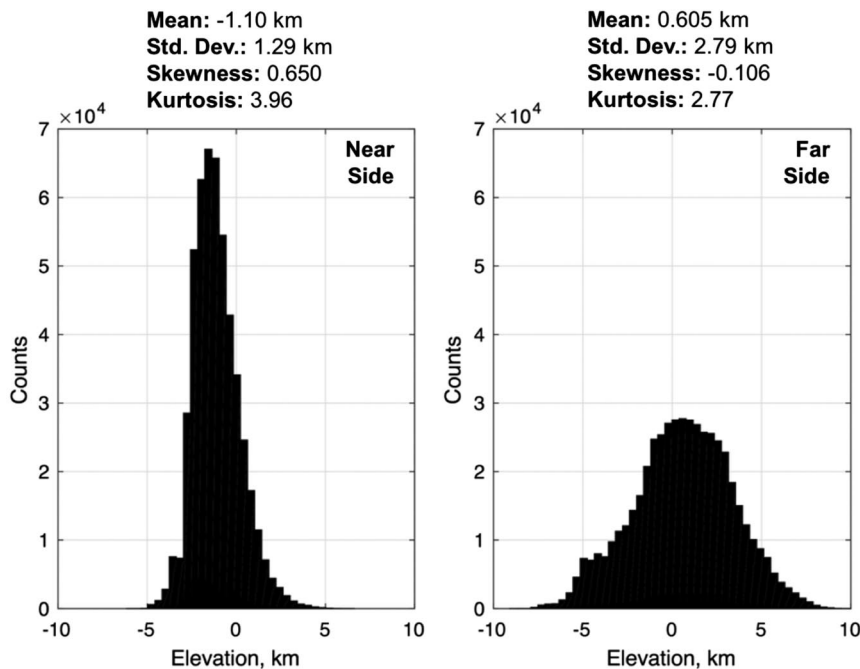


Fig. 9 Histograms of elevation on the near side (left) and far side (right) of the Moon.

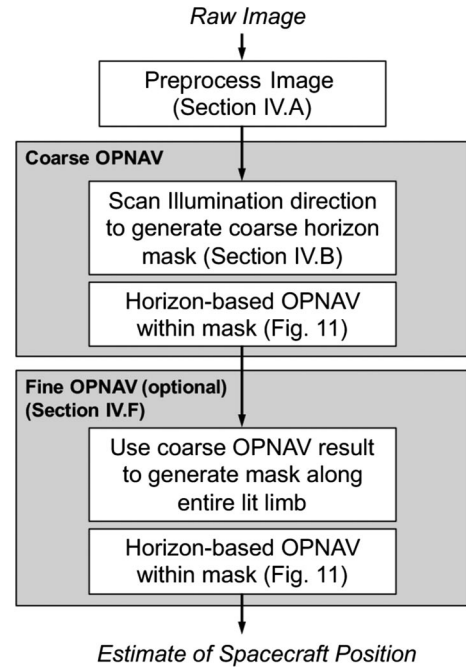


Fig. 10 Flowchart of entire horizon-based OPNAV procedure.

IV. Optical Navigation with Accurate Limb Localization in a Digital Image

With an OPNAV estimation algorithm (Sec. II.B) and a physical understanding of appearance of the planetary limb in an image (Sec. III) in hand, it is now possible to intelligently extract limb points from an image. An overview of the entire OPNAV procedure is shown in Fig. 10, and the core OPNAV process is further highlighted in Fig. 11. These flowcharts serve as a roadmap for the subsections that follow.

A. Image Preprocessing

Some basic preprocessing is necessary to prepare a raw image for use in a precision OPNAV algorithm. Although performing at least the following three preprocessing steps is recommended, additional steps may be required for images of especially low quality.

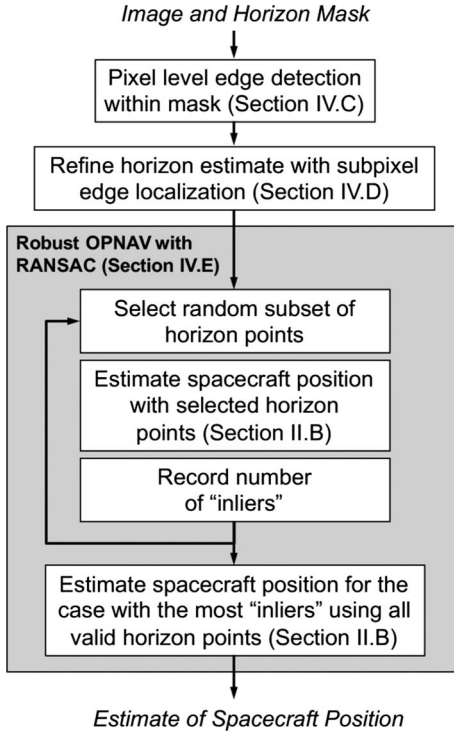


Fig. 11 Flowchart of core OPNAV process.

First, fixed pattern noise is removed from the image by subtracting the intensity bias at each pixel location from the raw intensity value. The intensity bias is determined by capturing a dark frame. If the camera has a mechanical shutter, a dark frame may be acquired by taking an image of the appropriate exposure with the shutter closed. If the image has an electronic shutter (as is the case with many modern digital cameras), an ensemble of star field images may be taken and the median value used for the dark frame.

Second, bad pixels are corrected. Radiation, launch vibrations, and other environmental effects often cause a few pixels on the focal plane to fail. These pixels may be identified, and their erroneous intensity values may be replaced using interpolation from adjacent pixels. The choice was made to correct these pixels by interpolation (rather than simply ignoring them) to better accommodate the region-based techniques used for subpixel edge localization.

Third, both lens aberrations and imperfections in manufacturing/assembly cause the apparent location of objects in an image to systematically deviate from the ideal pinhole camera location. Such distortions are well modeled using the Brown location model [77,78] and can be estimated with an accuracy suitable for spacecraft OPNAV applications using images of star fields [35]. This parametric model may be used to undistort the raw image. The author has found good results using simple bilinear interpolation in the undistortion process, although more sophisticated interpolation algorithms may be useful in some cases.

B. Coarse Horizon Mask from Illumination Scans

The lit limb of an ellipsoidal planet or moon will always be on the sunward side of the body. Further, the lit limb's projection onto an image will never appear to subtend greater than 180 degrees of horizon arc. These facts, coupled with the assumption that the sun is very far away, may be used to both accelerate and constrain the limb finding process.

At any point in time, the observed body's heliocentric position \mathbf{x} may be accurately obtained using known ephemerides [79]. This provides a vector going from the center of the sun to the center of the planet or moon and thus provides the illumination direction. Typical ephemerides are provided in an inertial frame (e.g., J2000), and so these must be rotated into the camera frame:

$$\mathbf{x}_C = \mathbf{T}_C^I \mathbf{x}_I \quad (36)$$

where \mathbf{T}_C^I is the 3×3 rotation matrix describing the rotation from the inertial frame to the camera frame.

The apparent illumination direction in the image is found by projecting \mathbf{x}_C onto the image plane. Recalling that the camera frame's Z axis is along the camera boresight direction,

$$\begin{bmatrix} x_{\text{illum}} \\ y_{\text{illum}} \end{bmatrix} = \begin{bmatrix} 1 & 0 & 0 \\ 0 & 1 & 0 \end{bmatrix} \mathbf{x}_C \quad (37)$$

which may be normalized to find the 2×1 illumination unit vector in the image plane:

$$\mathbf{u}_{\text{illum}} = \frac{1}{\sqrt{x_{\text{illum}}^2 + y_{\text{illum}}^2}} \begin{bmatrix} x_{\text{illum}} \\ y_{\text{illum}} \end{bmatrix} \quad (38)$$

With the illumination direction known, the image is now scanned along this illumination direction in search of the horizon. With the exception of a few special cases, the sunlight will appear to enter the scene from two of the image borders. Defining the border normals as \mathbf{b}_i (positive pointing into the image), a particular border is active if $\mathbf{b}_i^T \mathbf{u}_{\text{illum}} > 0$.

Proceed by initializing a horizon mask with all zeros. Then, for each active border, step along the border at a specified interval and scan the original image along the illumination direction $\mathbf{u}_{\text{illum}}$. Along each scan line, a persistent discontinuity in image intensity is sought. Specifically, each scan seeks the first time that n consecutive pixels are above a specified threshold. The step width n is chosen to avoid falsely triggering on bright stars, noise spikes, hot pixels, or debris. When an extended bright object is encountered, the mask is then set to 1 for each pixel in a 5×5 window about the intensity step location. The scanning procedure is shown graphically in Fig. 12.

C. Pixel-Level Horizon Localization

Horizon localization is a two step process. First, the approximate edge location is found using one of a number of existing pixel-level techniques. Second, this edge location is refined with a novel subpixel technique introduced in Sec. IV.D. Therefore, the discussion starts with a brief review of edges and with approaches for pixel-level horizon localization within the coarse mask generated by the illumination scans.

A body with no atmosphere presents a crisp horizon that would very nearly appear as an intensity step function in an image captured by a camera with an infinitely high resolution and a perfect lens. Such an ideal system, however, does not exist, and all real images of planets and moons exhibit an intensity gradient across the lit limb.

In a real image, the strength of the horizon edge depends on the apparent brightness at each point along the limb (or, more specifically, the size of the intensity step from space to planet) and the width of the

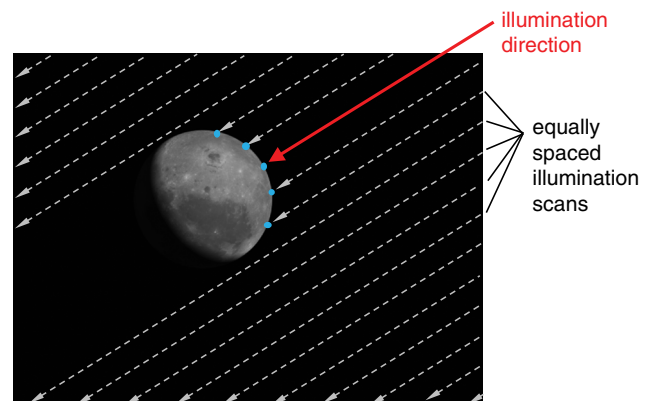


Fig. 12 Graphical depiction of the illumination scan technique used to accelerate limb finding and construct the coarse horizon mask. The blue dots show the candidate horizon points returned by the scans.

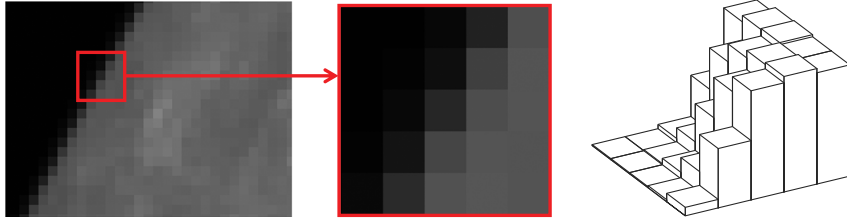


Fig. 13 Image intensity variation across a horizon edge as both an image (center frame) and a bar chart (right frame).

horizon transition depends on the camera PSF. The PSF for most well-built cameras is very nearly Gaussian [80,81], such that the observed image resembles the convolution of the ideal image with a 2-D Gaussian kernel. For the moment, assume that this symmetric Gaussian PSF is given by the kernel G , such that the observed image I is

$$I \approx G \star I_{\text{ideal}} \quad (39)$$

where \star is the image convolution operator. The end result is the type of blurred horizon edge seen in most real images. An example is shown in Fig. 13, where the image intensity inside of a 5×5 window centered about a candidate edge location is shown as an image and as a bar chart.

A variety of well-studied techniques exists for pixel-level edge localization [82,83]. Among the simplest techniques are those that find the image gradient through convolution with predefined templates and then search for extrema in the result, with the most common being the methods of Roberts [84], Prewitt [85], and Sobel [86]. Other popular techniques include those of Marr and Hildreth [also known as Laplacian of Gaussian (LoG) edge finding] [87] and Canny [88]. Newer algorithms, such as phase congruency [89,90], have also become popular in certain applications. The performance of these algorithms was assessed on a variety of planet images (for an example, see numerical results in Sec. IV.D.5 and Table 2). The Prewitt and Sobel edge detectors were found to perform the best, and the Sobel edge detector was selected for the present application.

Therefore, the Sobel edge detector is used to find edges that exist within the coarse horizon mask. The result is a set of candidate horizon points at integer pixel locations, $\{\tilde{u}_i, \tilde{v}_i\}_{i=1}^m$.

D. Subpixel Horizon Localization

Given m candidate horizon points located at integer pixel locations, $\{\tilde{u}_i, \tilde{v}_i\}_{i=1}^m$, the goal is now to refine these edge location estimates to obtain subpixel accuracy.

There is significant prior literature on finding the subpixel location of an edge in a digital image [89–101]. These techniques can loosely be divided into four categories: moment-based techniques [93–98], least-squares model fitting [27,99], interpolation [100], and the partial area effect [101]. Many of these techniques were attempted (see Sec. IV.D.5), and the partial area effect (PAE) method of Trujillo-Pino et al. [101] performed the best of the preexisting methods on the OPNAV problem. Despite this, it was subsequently found that a novel moment-based subpixel edge localization technique outperforms all previously existing methods (including the PAE method) for the specific task of accurate horizon localization. Again, see Sec. IV.D.5 for a performance comparison.

Therefore, a new moment-based technique is proposed for subpixel edge localization that is particularly well suited for OPNAV applications. This new technique, which is derived and discussed in the subsequent subsections, was chosen for four primary reasons. First, the solution is both analytic and noniterative, which makes this approach amenable to real-time implementation on a typical spacecraft flight computer. Second, the accuracy of subpixel edge localization is excellent, especially when compared to other methods of comparable algorithmic complexity. Third, the new method provides fast and robust estimations of the edge normal direction, which may be used to help screen candidate horizon points. Fourth, because each edge point is determined with subpixel accuracy using only pixels in a small region around that

specific edge point, the new method easily handles the gradual intensity variation along the lit limb arising from global changes in illumination/viewing geometry and local changes in albedo.

Although this paper presents a novel subpixel edge detection algorithm that results in notable performance improvements, any reasonable subpixel edge detector may be used (although less accurate edge localization results in less accurate OPNAV estimates). Consequently, the specific method selected may vary depending on the particular application or the user's preferences or experience.

The subsections that follow describe the development of the new edge localization method in a step-by-step manner. First, some important coordinate systems and a mapping between an image coordinate and the unit circle (within which the moments are defined) are introduced. Second, the edge model used in existing moment-based techniques is reviewed, and an alternative is presented. Third, the concept of orthogonal image moments for subpixel edge localization is applied to the new edge model. Fourth, the results for a continuous function are adapted to a digital image. Fifth, and finally, numerical results from the new technique are compared against 11 existing edge localization methods (five pixel-level methods and six subpixel-level methods).

1. Relation Between Images and Moments Defined Within the Unit Circle

Most moment-based edge localization techniques work by computing a handful of low-order moments defined within the unit circle and then use the relative values of these moments to infer the orientation and location of the edge (more on this in Sec. IV.D.3). Any point within this unit circle may be related to a point on a corresponding $N \times N$ pixel mask by a simple scaling of $N/2$. This concept is now briefly expanded in a more explicit manner.

Suppose that the pixel-level edge detection has identified a set of candidate horizon points located at integer pixel locations $\{\tilde{u}_i, \tilde{v}_i\}_{i=1}^m$. Now, consider the edge corresponding to any one of these candidate horizon points. Center an $N \times N$ mask (typically assume either a 5×5 mask or a 7×7 mask) about the pixel coordinate $\{\tilde{u}_i, \tilde{v}_i\}$ and inscribe a circle within this mask (see Fig. 14). Now define a new coordinate system whose origin is at $\{\tilde{u}_i, \tilde{v}_i\}$ with lengths scaled by $2/N$:

$$\bar{u} = \frac{2}{N}(u - \tilde{u}_i) \quad \bar{v} = \frac{2}{N}(v - \tilde{v}_i) \quad (40)$$

This creates a linear mapping from any point within the shaded portion of the mask in Fig. 14 to a corresponding point within the unit circle. The fact that some of the pixels in the $N \times N$ square mask (such as those around the edges) are not entirely contained within the unit circle is a topic that will be revisited in Sec. IV.D.4.

The specific example shown in Fig. 14 is a 5×5 mask centered about the candidate edge point $\{\tilde{u}_i, \tilde{v}_i\}$, within which a circle with a radius of 2.5 pixels is inscribed. Thus, because $\bar{u}^2 + \bar{v}^2 \leq 1$, there is a scaling of $2/N = 2/5 = 0.4$ to transform from the original pixel coordinates $\{u, v\}$ into the normalized coordinates $\{\bar{u}, \bar{v}\}$. The moments are only defined within the gray shaded region where $\bar{u}^2 + \bar{v}^2 \leq 1$. Thus, the information in the extreme corners of the square $N \times N$ mask is ignored. Operating only within the circular mask (and ignoring the corners of the square mask) is necessary to achieve the rotational invariance required to find the location of an edge at an arbitrary orientation within the original image.

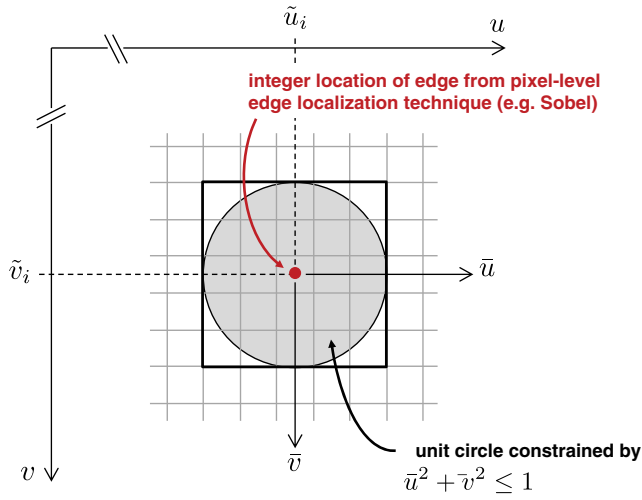


Fig. 14 Definition of coordinate frames and mask for moment-based edge localization.

2. Alternate Edge Model

Most of the existing literature on moment-based subpixel edge localization assumes a simple intensity step function defined within the unit circle as shown in the top diagram in Fig. 15. This model assumes that a discontinuity in image intensity occurs at a distance l from the center of the unit circle. The step function model was put forward by Lyvers et al. in [93] and has since been used without substantial critique by a variety of other authors [94–98].

Real images (especially those used for OPNAV, which often have a small amount of intentional defocus) do not exhibit an intensity step function across an edge. Instead, as was discussed earlier, the lens PSF and image digitization cause the intensity to change gradually over a finite width. A careful study of moment-based techniques will show that the simple step function model introduces a bias in the edge location if the edge in the actual image changes gradually. This bias was also observed by Lyvers et al. in [93], where they considered a two-level intensity function in an attempt to quantify the bias introduced by image digitization. Therefore, the author found it necessary to develop a different model for the intensity profile across an edge (which is often called the edge spread function, ESF).

If the camera PSF is well approximated by a 2-D Gaussian, then the ideal ESF should resemble the cumulative distribution function (CDF) of a Gaussian:

$$I(\bar{u}') = h + k \frac{1}{2} \left[1 + \operatorname{erf} \left(\frac{\bar{u}' - l}{\sigma\sqrt{2}} \right) \right] \quad (41)$$

where \bar{u}' is the position along an axis perpendicular to the edge (the l symbol is used to indicate a position in the frame aligned with the edge), l is the edge location, and σ controls the edge width. Unfortunately, this edge model prevents analytic evaluation of the moments, and a somewhat simpler model is needed. Therefore, the author proposes to model the ESF with an intensity ramp governed by

$$I(\bar{u}') = \begin{cases} h & \bar{u}' \leq l - w \\ h + k[\bar{u}' - (l - w)]/(2w) & l - w < \bar{u}' < l + w \\ h + k & \bar{u}' \geq l + w \end{cases} \quad (42)$$

where $2w$ is the full edge width. It was found that $w \approx 1.66\sigma$ provides a good approximation of the Gaussian ESF, and an example is shown in Fig. 16. This example assumes an edge at $l = 0.3$ with $\sigma = 0.2$, $h = 40$, and $k = 155$. The linear ramp model has an edge width of $w = 1.66\sigma = 0.332$.

This intensity ramp function may be used to replace the intensity step function as the edge model, where both are defined only within the unit circle (see Fig. 15).

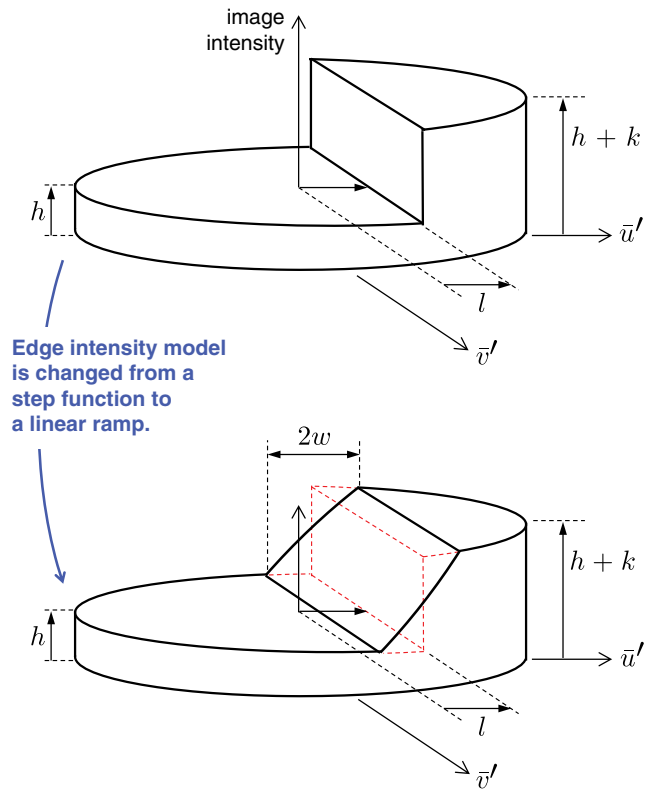


Fig. 15 The classic step function edge model (top diagram) is replaced with a linear ramp edge model (bottom diagram). Both are only defined within the unit circle.

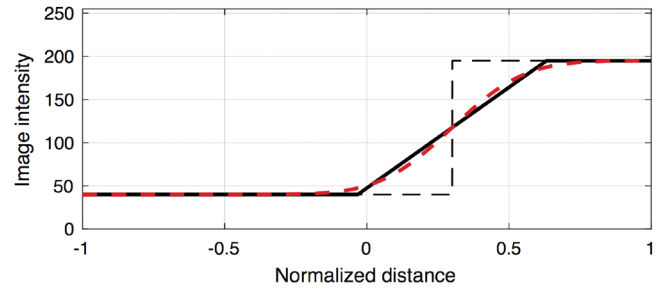


Fig. 16 Comparison of the ESF for a perfect step function (dashed black line), Gaussian CDF (dashed red line), and a linear ramp (solid black line).

3. Moment-Based Edge Localization for a Continuous Signal

With a revised ESF model in hand, it is now necessary to select the appropriate moments and determine their relationship to the edge location. The use of moment-based techniques for subpixel localization is well established, with a variety of methods using standard moments [93], Zernike moments [94,95], and Fourier–Mellin moments [96–98]. As will be shown shortly, moment-based techniques make use of integral operators and tend to be less sensitive to uncorrelated image noise than gradient-based techniques.

Despite some literature claiming that orthogonal Fourier–Mellin moments (OFMMs) are superior to the orthogonal Zernike moments for subpixel edge localization [96–98], a brief analysis will show that these two techniques are analytically and numerically equivalent. (It is noted, however, that OFMMs do have a number of real advantages for the more general problem of pattern recognition [102].) Thus, there is absolutely no difference between the edge location predicted by Zernike moments and by OFMMs. This fact is shown in Appendix B and further borne out by numerical experiments presented later in this paper. Therefore, the present analysis proceeds with the use of Zernike moments for two reasons. First, the integrals are easier to analytically evaluate. Second, fewer moments are

required to obtain the edge location estimate, thus reducing computation time on a digital computer.

The use of Zernike moments for subpixel edge localization with a step-function edge model is discussed in detail by Ghosal and Mehrotra in [94]. Here, just enough of this prior work is reviewed to extend their results to the intensity ramp edge model introduced previously.

The Zernike moment of order n and repetition m for the 2-D signal $f(\bar{u}, \bar{v})$ is defined within the unit circle as

$$Z_{nm} = \frac{n+1}{\pi} \iint_{\bar{u}^2 + \bar{v}^2 \leq 1} f(\bar{u}, \bar{v}) T_{nm}(r, \theta) d\bar{u} d\bar{v} \quad (43)$$

where $T_{nm}(r, \theta)$ is the Zernike moment kernel function expressed in polar coordinates: $r^2 = \bar{u}^2 + \bar{v}^2$ and $\tan \theta = \bar{v}/\bar{u}$. Furthermore, these kernel functions are defined as

$$T_{nm}(r, \theta) = R_{nm}(r) \exp(jm\theta) \quad (44)$$

where $j = \sqrt{-1}$ and the orthogonal polynomials $R_{nm}(r)$ are defined as

$$R_{nm}(r) = \sum_{s=0}^{(n-|m|)/2} \frac{(-1)^s (n-s)! r^{n-2s}}{s! \left(\frac{n+|m|}{2} - s\right)! \left(\frac{n-|m|}{2} - s\right)!} \quad (45)$$

which evaluate to

$$R_{00}(r) = 1 \quad (46)$$

$$R_{11}(r) = r \quad (47)$$

$$R_{20}(r) = 2r^2 - 1 \quad (48)$$

\vdots

and, in turn, lead to Zernike kernel functions of (results are converted from polar coordinates to Cartesian coordinates for easier integration)

$$T_{00}(r, \theta) = T_{00}(\bar{u}, \bar{v}) = 1 \quad (49)$$

$$T_{11}(r, \theta) = T_{11}(\bar{u}, \bar{v}) = \bar{u} + j\bar{v} \quad (50)$$

$$T_{20}(r, \theta) = T_{20}(\bar{u}, \bar{v}) = 2\bar{u}^2 + 2\bar{v}^2 - 1 \quad (51)$$

\vdots

It is common practice to define just the integral term in Eq. (43) as A_{nm} :

$$A_{nm} = \iint_{\bar{u}^2 + \bar{v}^2 \leq 1} f(\bar{u}, \bar{v}) T_{nm}(\bar{u}, \bar{v}) d\bar{u} d\bar{v} \quad (52)$$

such that

$$Z_{nm} = \frac{n+1}{\pi} A_{nm} \quad (53)$$

Two key observations about Zernike moments may now be made.

First, consider an edge whose normal is oriented at an angle ψ with respect to the \bar{u} axis (Fig. 17). It is possible to relate the Zernike moments in the original coordinate system with the Zernike moments in a new coordinate system aligned with the edge's orientation, defined by the \bar{u}' and \bar{v}' coordinate axes (Fig. 17) such that $\theta' = \theta - \psi$. Given these angle definitions, it is easy to see that $\exp(jm\theta') = \exp(jm\theta) \exp(-jm\psi)$. Substituting this result into Eqs. (44) and (52) leads directly to

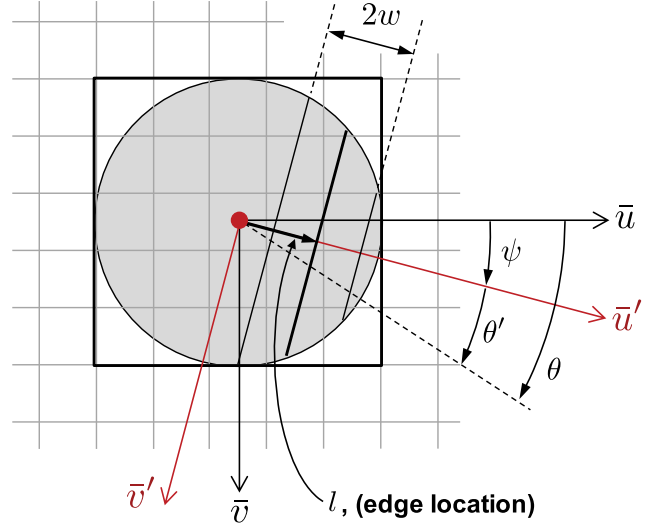


Fig. 17 Definition of edge orientation and important angles. The “primed” frame describes the frame aligned with the edge.

$$A'_{nm} = A_{nm} \exp(-jm\psi) \quad (54)$$

where A_{nm} is the Zernike moment of the original image (the \bar{u} - \bar{v} coordinate system), and A'_{nm} is the Zernike moment aligned with the edge (the \bar{u}' - \bar{v}' coordinate system).

Second, using the approach from [94], it is straightforward to show that

$$\text{Im}[A'_{11}] = 0 \quad (55)$$

Therefore, considering the imaginary component of A'_{11} , apply Eq. (54), and recall that $\exp(-jm\psi) = \cos(m\psi) - j \sin(m\psi)$ to find

$$\psi = \text{atan2}(\text{Im}[A_{11}], \text{Re}[A_{11}]) \quad (56)$$

Thus, the orientation of the edge may be found using only a single Zernike moment: A_{11} .

With these two observations in hand, the remaining task is to determine the distance of the edge from the center of the unit circle. To avoid confusion, the edge location for the step model is defined as l_s , where the subscript s is used to distinguish this result from the estimate using the linear ramp. For an edge modeled as a step function, the integrals for A'_{11} and A'_{20} may be solved analytically and have simple results [94]:

$$A'_{11} = \frac{2k(1 - l_s^2)^{3/2}}{3} \quad (57)$$

$$A_{20} = A'_{20} = \frac{2kl_s(1 - l_s^2)^{3/2}}{3} \quad (58)$$

This permits an easy solution for l_s :

$$l_s = \frac{A_{20}}{A'_{11}} \quad (59)$$

where the earlier result for ψ is used to find A'_{11} from the moment calculated in the original (unrotated) image:

$$A'_{11} = \text{Re}[A_{11}] \cos \psi + \text{Im}[A_{11}] \sin \psi \quad (60)$$

Thus, the edge location for a perfect intensity step may be found using only two moments (A_{11} and A_{20}) along with the angle ψ [which was computed from A_{11} using Eq. (56)]. Unfortunately, as was mentioned in

Sec. IV.D.2, Eq. (59) does not produce a good estimate of the edge location if the true underlying signal has a gradually changing edge.

Therefore, replace the step function edge model with the linear ramp edge model from Eq. (42). This new edge model also permits the integrals for the moments A'_{11} and A'_{20} to be found analytically:

$$A'_{11} = \frac{k}{24w} \{ 3\sin^{-1}(l+w) - 3\sin^{-1}(l-w) - (5(l-w) - 2(l-w)^3)(1-(l-w)^2)^{1/2} + (5(l+w) - 2(l+w)^3)(1-(l+w)^2)^{1/2} \} \quad (61)$$

$$A'_{20} = A'_{20} = \frac{k}{15w} [(1-(l-w)^2)^{5/2} - (1-(l+w)^2)^{5/2}] \quad (62)$$

A few intermediate steps for finding these integrals are provided in Appendix C. Each of these results was validated via numerical integration on a wide array of different examples. It is also reassuring to observe that the moments from Eqs. (61) and (62) approach the simple step function results [Eqs. (57) and (58)] as w goes to zero. That is,

$$\lim_{w \rightarrow 0} A'_{11} = \frac{2k(1-l^2)^{3/2}}{3} \quad (63)$$

$$\lim_{w \rightarrow 0} A'_{20} = \frac{2kl(1-l^2)^{3/2}}{3} \quad (64)$$

The new analytic expressions for the Zernike moments in Eqs. (61) and (62) are now much more complicated than for the step function case and no longer permit an easy path to a closed-form solution for the edge location. Indeed, even the simpler two-level edge model with simpler moments that was investigated in [93] did not produce a closed-form solution for the edge location (Lyvers et al. suggested a precomputed lookup table as a solution to this problem).

Although an exact and closed-form solution for l has evaded us thus far, a very good approximation may be made (and this approximation is found to be sufficiently good that the continued pursuit of an exact analytic solution is of little practical value). Specifically, the edge location for the ramp model, l , may be approximately related to the two Zernike moments by the empirical relation

$$\frac{A'_{20}}{A'_{11}} \approx l[1 - (1+l/2)w^2] \quad (65)$$

which may be analytically solved for l (retaining only the desired solution):

$$l = \left[1 - w^2 - \sqrt{(w^2 - 1)^2 - 2w^2 A'_{20}/A'_{11}} \right] / w^2 \quad (66)$$

where A'_{11} may be computed according to Eq. (60).

Importantly, observe that

$$\lim_{w \rightarrow 0} l = A'_{20}/A'_{11} = l_s \quad (67)$$

which shows that the solution from Eq. (66) approaches the step function solution from Eq. (59) as w goes to zero.

In summary, the result for ψ from Eq. (56) allows for straightforward computation of the edge normal direction in the image plane:

$$\mathbf{n} = \begin{bmatrix} n_u \\ n_v \end{bmatrix} = \begin{bmatrix} \cos \psi \\ \sin \psi \end{bmatrix} \quad (68)$$

Furthermore, using ψ and the estimate of l from Eq. (66), the edge location in the normalized coordinate system is found to be

$$\begin{bmatrix} \tilde{u} \\ \tilde{v} \end{bmatrix} = l \begin{bmatrix} \cos \psi \\ \sin \psi \end{bmatrix} \quad (69)$$

which may be used to find the subpixel edge location in the original image through the application of Eq. (40),

$$\begin{bmatrix} u_i \\ v_i \end{bmatrix} = \begin{bmatrix} \tilde{u}_i \\ \tilde{v}_i \end{bmatrix} + \frac{Nl}{2} \begin{bmatrix} \cos \psi \\ \sin \psi \end{bmatrix} \quad (70)$$

To better see the improvement in edge localization provided by Eq. (66), consider a 5×5 pixel mask mapped to the unit circle. Within this mask, all reasonably plausible edge scenarios were considered, and contours of edge localization errors are shown in Fig. 18. Specifically, the edge location was varied from 0 to 1 pixel, and the edge width was varied from 0 to 1.9 pixels. These ranges are quite conservative, given the maximum observed errors for the Sobel edge detector and typical image PSFs. The gray region in the top-right corner of Fig. 18 is where the upper edge of the intensity ramp becomes too close to the boundary of the unit circle.

Figure 18 highlights the significant gains realized by the new approach proposed here. The solution for the new method is better than 0.015 pixels everywhere, whereas the step function edge model can have errors as high as 0.35 pixels. Compared with the classic step function edge model, the result of the new method is an order of magnitude better everywhere and multiple orders of magnitude better over most of the domain. In both cases (old method and new method), the error approaches zero as w goes to zero.

4. Application to a Digital Image

The preceding discussions considered continuous functions that were exactly integrated. Instead, consider a digital image with data existing only at integer pixel locations. Replace the Zernike moment double integral in Eq. (52) with a double summation (a 2-D correlation)

$$A_{nm} \approx \sum_{k=-p}^p \sum_{j=-p}^p I(\tilde{u}_i + j, \tilde{v}_i + k) M_{nm}(p + j, p + k) \quad (71)$$

where $p = (N - 1)/2$, and N is assumed to be an odd integer. The value of each entry in the correlation mask M_{nm} is found by integrating T_{nm} over the corresponding pixel and within the unit circle:

$$M_{nm}(j, k) = \iint_{\substack{\tilde{u}^2 + \tilde{v}^2 \leq 1 \\ \tilde{u} = \tilde{u}_i + j, \tilde{v} = \tilde{v}_i + k}} T_{nm}(\tilde{u}, \tilde{v}) d\tilde{u} d\tilde{v} \quad (72)$$

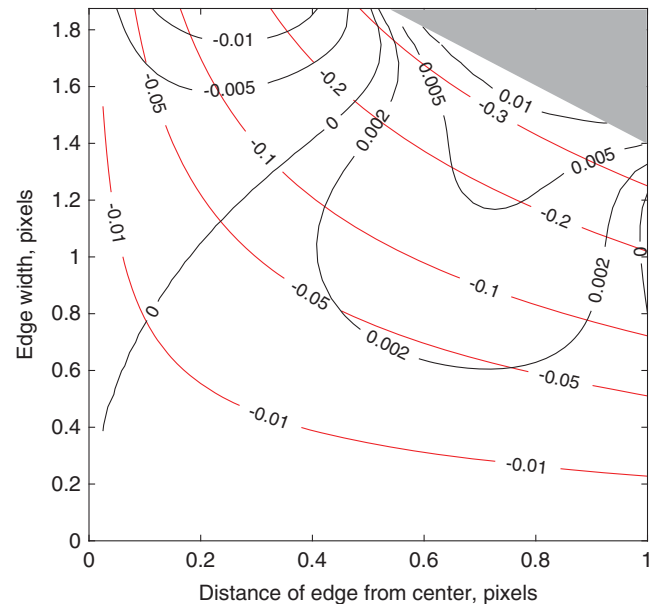


Fig. 18 Contours of edge localization error in pixels for the classic Zernike moment approach from [94] (red) and for the new Zernike moment approach presented in this paper (black).

where A_{jk} is the area of the pixel $\{j, k\}$ that is contained within the unit circle. For pixels in the center of the mask, A_{jk} is the entire pixel. For pixels toward the edge of the mask, A_{jk} is only the portion of the pixel within the unit circle (which is the smallest for corner pixels). Thus, image information outside of the unit circle is “ignored” in practice by populating the correlation mask with values computed only within the unit circle (which effectively assumes a zero weight outside of the unit circle). Therefore, the Zernike moments for an image I may be found by

$$A_{nm} = M_{nm} * I \quad (73)$$

where $*$ is the image correlation operator.

Note that the mask M_{11} is complex valued, whereas the mask M_{20} is real valued. A few observations on M_{11} will make implementation easier and more efficient. First, by definition,

$$M_{11} = \text{Re}[M_{11}] + j\text{Im}[M_{11}] \quad (74)$$

A careful study of Eq. (72) and the structure of $T_{nm}(\bar{u}, \bar{v})$ reveals that the mask for the imaginary component of M_{11} is simply the transpose of the real component of M_{11} . That is,

$$\text{Im}[M_{11}] = \text{Re}[M_{11}]^T \quad (75)$$

This makes intuitive sense if one considers how the ratio of the imaginary and real components of A_{11} may be used to find the edge orientation in Eq. (56). Consequently, it is only necessary to carry the real component of M_{11} . Applying this allows the computation of A_{11} to be split into two correlations:

$$A_{11} = \text{Re}[A_{11}] + j\text{Im}[A_{11}] \quad (76)$$

where

$$\text{Re}[A_{11}] = \text{Re}[M_{11}] * I \quad (77)$$

$$\text{Im}[A_{11}] = \text{Re}[M_{11}]^T * I \quad (78)$$

Likewise, the computation of A_{20} (which has only real components) is given by

$$A_{20} = M_{20} * I \quad (79)$$

Thus, subpixel edge finding requires three correlations: two for A_{11} and one for A_{20} . Then, at each pixel-level edge location, the corrected edge location is found by applying the result of these three correlations to Eqs. (56), (66), and (70).

One final observation is now warranted. Because the underlying Zernike kernel functions T_{nm} are unchanged relative to earlier work (only the edge model changed, and hence the relation of these moments to the edge location changed), the resulting correlation masks generated by Eq. (72) are also unchanged. Thus, the masks needed are the same as those presented in [94] for the 5×5 case, although this work is structured to only require the real component of M_{11} due to the relation in Eq. (75). This work also uses a different sign convention for the edge orientation from that in [94], which allows for more

Table 2 Performance comparison of edge detection techniques for planetary limb localization

Method	Edge localization error, pixels		
	Mean	Standard deviation	Maximum
Roberts [84]	0.129	0.526	1.251
Prewitt [85]	0.015	0.280	0.577
Sobel [86]	0.016	0.281	0.608
Marr and Hildreth (LoG) [87]	0.487	0.276	1.162
Canny [88]	0.034	0.344	0.726
Lyvers et al. [93]	0.017	0.135	0.368
Ghosal and Mehrotra [94]	0.012	0.137	0.340
Jensen and Anastassiou [92]	-0.001	0.256	0.758
Ying-Dong et al. [95]	0.027	0.100	0.313
Tan et al. [96] and Bin et al. [97]	0.012	0.137	0.340
Trujillo-Pino et al. [101]	0.036	0.098	0.327
Christian (this paper)	0.020	0.063	0.242

straightforward analysis. For the convenience of the reader, the Zernike masks were computed and are provided in Fig. 19 for the 5×5 case and in Fig. 20 for the 7×7 case. In these figures, the mask pixels are shaded from black (most negative) to white (most positive) to give the reader an intuitive sense of how each kernel weights the image data. The values in these figures are constants for a particular choice of mask size, regardless of application or other problem parameters.

5. Brief Comparison of Edge Localization Methods

A variety of edge localization methods were evaluated for finding the horizon edge in the simulated Moon image from Fig. 1, with a comparison of results presented in Table 2. The top set of results are pixel-level edge finding techniques, and the bottom set of results are subpixel edge finding techniques. All of the subpixel methods in Table 2 are functionally zero-mean (providing an unbiased estimate of the limb location) and significantly outperform the pixel-level techniques. Unsurprisingly, the results of the OFMM technique (Tan et al. [96] and Bin et al. [97]) are exactly the same as the simpler Zernike moment technique (Ghosal and Mehrotra [94]) for the reasons discussed in Sec. IV.D.3 and in Appendix B. It was found that the method of Trujillo-Pino et al. [101] is the best of the preexisting methods and that the new technique presented in this paper provides substantial further improvement. More detailed statistics are provided for the PAE method and the new moment-based method in Fig. 21.

The exact geometric distance between the measured horizon points and the true horizon ellipse (which is perfectly known because this is a simulated image) is found using the technique presented in [24].

E. Robust Horizon Fitting with Random Sample Consensus

A variety of real-world effects may cause some of the m measured horizon points to not precisely lie on the horizon. Although the root cause of these errors comes from a wide range of sources, such as extreme albedo variations or unexpected radiation artifacts, they may all be handled in a similar manner through robust estimation techniques. A random sample consensus (RANSAC) [103] approach was found to be adequate. The specific approach used here is as follows.

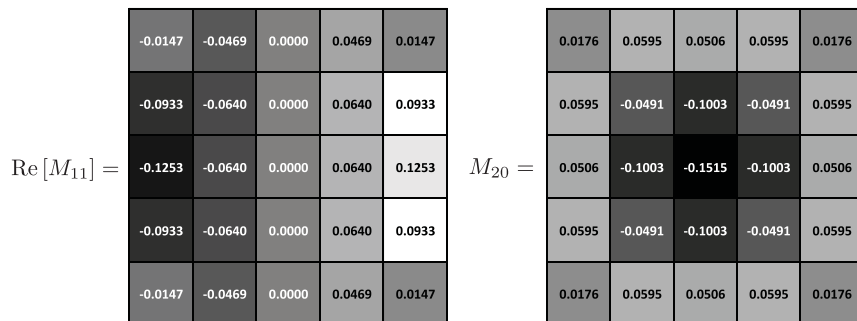


Fig. 19 Values for Zernike masks of size 5×5

$\text{Re}[M_{11}] =$	0.0000	-0.0150	-0.0190	0.0000	0.0190	0.0150	0.0000
	-0.0224	-0.0466	-0.0233	0.0000	0.0233	0.0466	0.0224
	-0.0573	-0.0467	-0.0233	0.0000	0.0233	0.0467	0.0573
	-0.0690	-0.0467	-0.0233	0.0000	0.0233	0.0467	0.0690
	-0.0573	-0.0467	-0.0233	0.0000	0.0233	0.0467	0.0573
	-0.0224	-0.0466	-0.0233	0.0000	0.0233	0.0466	0.0224
	0.0000	-0.0150	-0.0190	0.0000	0.0190	0.0150	0.0000

$M_{20} =$	0.0000	0.0225	0.0394	0.0396	0.0394	0.0225	0.0000
	0.0225	0.0271	-0.0128	-0.0261	-0.0128	0.0271	0.0225
	0.0394	-0.0128	-0.0528	-0.0661	-0.0528	-0.0128	0.0394
	0.0396	-0.0261	-0.0661	-0.0794	-0.0661	-0.0261	0.0396
	0.0394	-0.0128	-0.0528	-0.0661	-0.0528	-0.0128	0.0394
	0.0225	0.0271	-0.0128	-0.0261	-0.0128	0.0271	0.0225
	0.0000	0.0225	0.0394	0.0396	0.0394	0.0225	0.0000

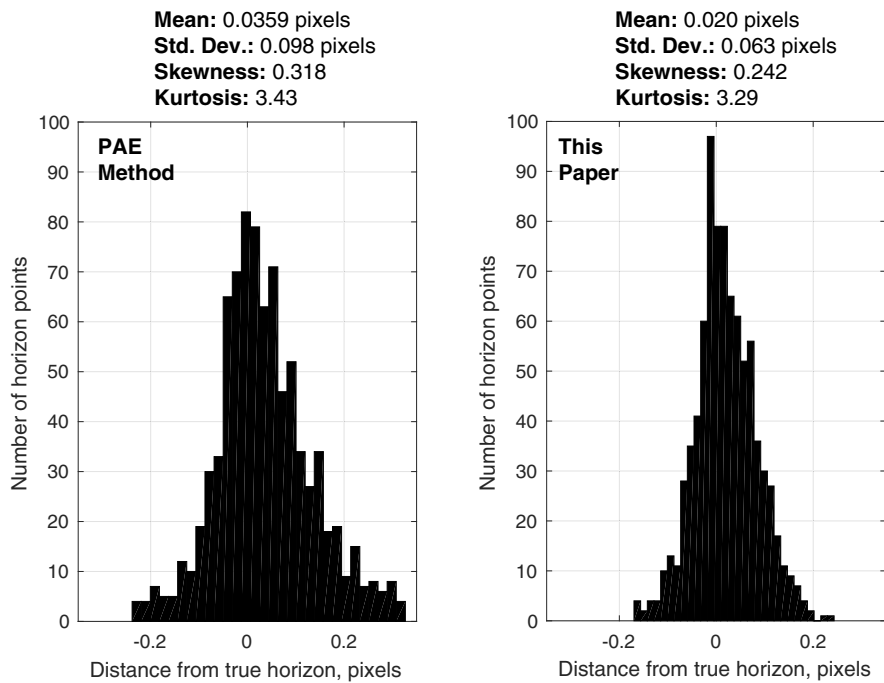
Fig. 20 Values for Zernike masks of size 7×7 .

Fig. 21 Histograms of edge localization errors for the PAE technique (left) and for the new technique presented in this paper (right).

Begin by randomly selecting n points (where $n \leq m$) from the set of m subpixel horizon points, $\{u_i, v_i\}_{i=1}^m$, found using Eq. (70). Convert the pixel coordinates into rays along the body's tightly bounding cone according to Eq. (8). Then, compute the position of the spacecraft using the noniterative OPNAV method presented in Sec. II.B. With an estimate of the spacecraft position in hand, reproject the expected horizon arc onto the image using Eq. (6) and count the total number of candidate horizon points within a specified tolerance (or "inliers"). Repeat this procedure for many different random combinations of candidate horizon points, keeping track of the solution that provided the most inliers.

Once all the random combinations of horizon points have been considered, take the inliers from the best match and use this entire set of points to recompute the spacecraft position with OPNAV solution from Sec. II.B.

F. Final Horizon Fit and Optical Navigation Position Estimate

Depending on the spacing between the illumination scans in Sec. IV.B, the sampling of the horizon within the coarse horizon mask may be somewhat sparse. As a result, the refined edge set found in Sec. IV.E also operates on this sparse horizon sampling. Although this can greatly speed up the initial processing, it may be desirable to

use the entire lit limb for the final OPNAV solution. This may be done in a few simple steps.

First, take the OPNAV solution from Sec. IV.E and reproject the horizon onto the image. Then, repeat the horizon localization procedure using all of the pixels that 1) are within k pixels of the reprojected horizon arc, and 2) are within an angle θ_{\max} of the illumination direction. The second criterion permits the horizon points near the luminance poles to be ignored, which can be problematic (see discussion in Sec. III.B). Finally, repeat the RANSAC procedure from before using this full set of horizon points.

Note, of course, that this final step is only necessary if the original illumination scans are sparse. If the original illumination scans are dense, there should be little practical difference between the family of horizon points generated in the coarse horizon mask and in the ellipse-based mask described in the preceding paragraph (assuming that the θ_{\max} check is incorporated into the final RANSAC estimate).

V. Practical Considerations and Numerical Results

A. Intensity Profiles Along the Lit Limb and Iterative Refinement of Horizon Location

The intensity profile along the lit limb is not a constant. As discussed in Sec. III.B, both global changes in illumination/viewing

geometry and local changes in albedo cause significant variation in apparent image intensity along the lit limb. The desire to avoid these complications was one rationale for selecting the new moment-based method, which finds the horizon with subpixel accuracy using the only pixels in the immediate neighborhood of each horizon point.

Now, it is sometimes possible to further improve limb localization for a smooth body through an iterative least-squares fit of the entire limb. Two recent examples of such an approach are [27,32]. Such approaches, however, typically assume a constant intensity along the entire lit limb, which is known from Figs. 5 and 6 to generally be a poor assumption for rough bodies with no atmosphere and with varying albedo (interestingly, however, the lit horizon of a body modeled by the Lommel–Seeliger law will have a constant intensity because $\cos e = 0$ along the horizon). Thus, because a constant intensity model is not supported by the data, this existing approach is abandoned for something slightly different.

Recall that a primary advantage of horizon-based OPNAV is that it does not require rendering of the expected intensity profile along the lit limb, which relies on precise knowledge of both the body's terrain and albedo. Therefore, consider an empirical data-driven approach instead of a predictive approach. More specifically, model the intensity gradient profile along the lit limb with the first few terms of a Fourier series:

$$G(\theta) = G_0 + \sum_{k=1}^n [a_k \cos(k\theta) + b_k \sin(k\theta)] \quad (80)$$

where θ is the angle along the lit limb as measured from the luminance equator (i.e., center of the lit horizon). Thus, by definition, $-90 \leq \theta \leq 90$ deg.

Further recall that the sharp edge along the horizon for a body with no atmosphere is blurred by the camera PSF. Thus, assuming that the PSF is well modeled by a Gaussian, the horizon ESF should create an intensity profile resembling the integral of a Gaussian [see Eq. (41) and related discussion]. Furthermore, a slice perpendicular to the limb of the image gradient should produce a Gaussian profile (this is often called the line spread function, LSF). Using such a model, a band of pixels around the horizon may be used to estimate the camera position, the PSF width, and the limb intensity profile via a standard iterative least-squares approach.

This type of iterative limb localization was performed on a synthetic image of a perfectly smooth Moon (shown in Fig. 22), and the final fit of the lit limb's intensity gradient profile is shown in Fig. 23. In this example, the iterative procedure was given an initial guess generated by the PAE method and reduced the maximum error in the reprojected ellipse from about 0.1 to 0.0628 pixels. The Moon radius in this image varies from 396.24 to 396.42 pixels, and so these errors correspond to a 0.025% error for the PAE method and a 0.016%



Fig. 22 Example OPNAV image of the Moon.

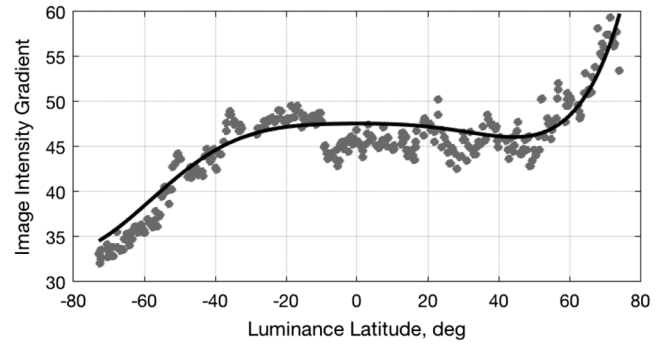


Fig. 23 Profile of intensity gradient along the lit limb of the Moon from Fig. 22. Gray dots are raw image data and black line is the fit produced by the iterative horizon localization routine.

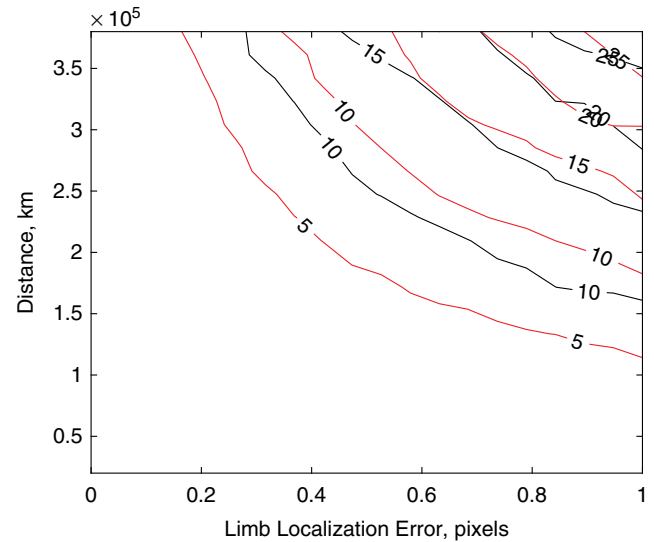


Fig. 24 Contours of cross-boresight OPNAV errors in kilometers for a smooth Moon (red lines) and for a rough moon (black lines).

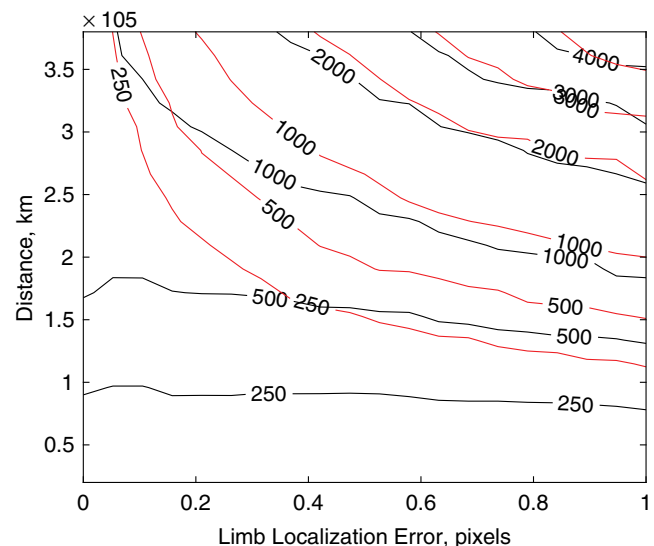


Fig. 25 Contours of along-boresight OPNAV errors in kilometers for a smooth Moon (red lines) and for a rough moon (black lines).

error after iterative refinement. The performance of this iterative technique appears to be functionally identical to the results presented by Mortari et al. in [27] for a substantially similar scenario.

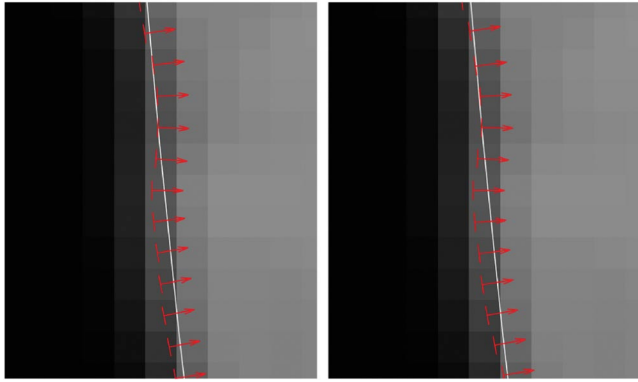


Fig. 26 Example horizon localization with the PAE method (left) and with the new moment-based method (right) for a body model with terrain.

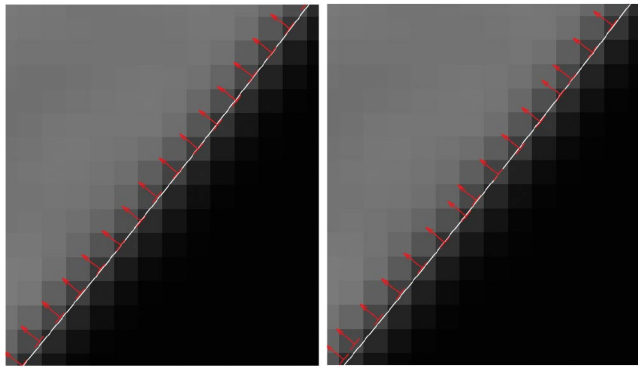


Fig. 27 Example horizon localization with the PAE method (left) and with the new moment-based method (right) for a smooth (no terrain) body model.

The new moment-based technique introduced in Sec. IV.D.3 of this paper produces a maximum error in the reprojected ellipse of 0.0630 pixels (effectively the same performance as the iterative techniques), but it achieves this accuracy without iteration and at a fraction of the computational cost. No further improvement is realized when the moment-based result is used as the initial guess for the iterative routine. Consequently, the author deems iterative improvement of the horizon fit to be unnecessary.

B. Terrain Variation Can Dominate Optical Navigation Performance

It is often the case that the smooth planet assumption (and not the accuracy of the horizon localization) drives the performance of horizon-based OPNAV. This is now illustrated by example. Suppose

that a camera with a 2048×2592 pixel focal plane and a 16×20 deg field of view (similar to the anticipated Orion OPNAV camera [35]) collects images of the Moon. Now, consider two models of the Moon. Let the first Moon model be perfectly smooth, and let the second Moon model have a 75-percentile terrain roughness (using the stochastic terrain model introduced in Sec. III.C).

Further suppose that these two models are imaged at distances from 20,000 to 380,000 km. Also, suppose that the accuracy of the edge localization process varies from 0.0 pixels (perfect limb localization) to 1.0 pixel. A Monte Carlo analysis of the entire estimation process was run on each combination of distance and limb localization accuracy. The resulting contours of end-to-end OPNAV performance are shown in Fig. 24 for the cross-boresight errors and in Fig. 25 for the along-boresight errors. A few very important observations may be made from these two contour plots.

First, the along-boresight errors are always greater than the cross-boresight errors. This is consistent with intuition and significant previous work in the area of horizon-based OPNAV covariance [30].

Second, the smooth Moon model has smaller errors than the rough Moon model, which is especially evident at closer distances. This is as expected because the OPNAV estimation procedure assumes a smooth body. Thus, the smooth Moon case has no modeling error in body shape within the estimation procedure, whereas the rough Moon case does have modeling error in the body shape.

Third, the errors for the smooth Moon model and rough Moon model become increasingly similar as the distance increases and as the limb localization error increases. This, again, is as expected. As either the distance or limb localization error increases, the relative contribution of the terrain becomes less. Because the terrain contributes less, there is less of a difference between the smooth and rough models, and their error becomes similar.

Fourth, terrain dominates at close distances, and there is very little sensitivity to the accuracy of limb localization in the image. This is especially true in the along-boresight direction. Note that the rough Moon model contours (black lines) in Fig. 25 are nearly horizontal (meaning that the changing limb localization error has no measurable impact on performance) for distances of less than about 200,000 km. This distance will be different if the camera is changed. Note, of course, that as the distance continues to increase, the Moon eventually becomes small enough that limb localization is more important than the terrain (as was discussed in the previous observation). At these extreme distances, however, images of the Earth may be more useful than images of the Moon.

C. Example Horizon Localization Results

The edge localization techniques presented in this paper were applied to a variety of planetary limb examples, and a few results are shown in Figs. 26 and 27. The first example (Fig. 26) shows results for a body model with terrain, whereas the second example (Fig. 27) shows results for a perfectly smooth body. In each case, the projection

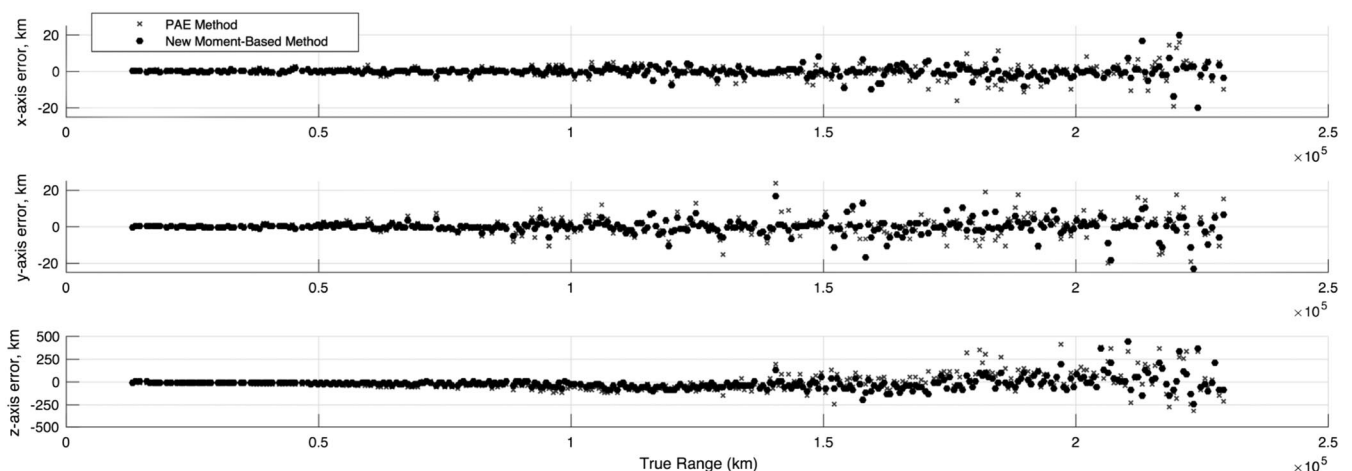


Fig. 28 Example OPNAV performance with a smooth Moon for two different horizon localization techniques.

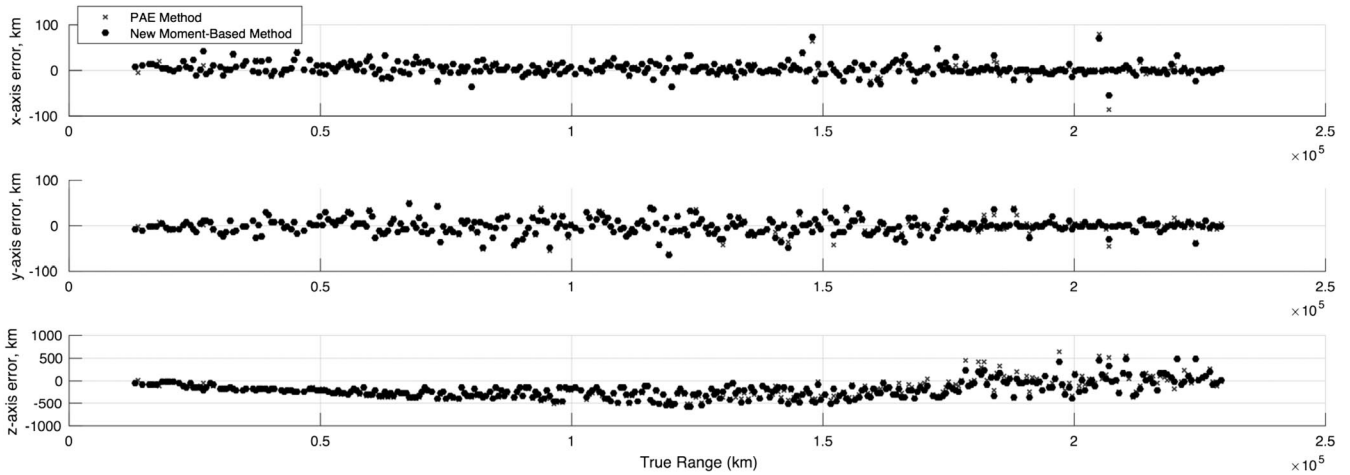


Fig. 29 Example OPNAV performance for a Moon with terrain for two different horizon localization techniques.

Table 3 RMS of distance-normalized OPNAV errors for results shown in Figs. 28 and 29

Horizon localization method	RMS of normalized errors	
	Smooth Moon (Fig. 28)	Moon with terrain (Fig. 29)
PAE method	0.00064	0.00311
New moment-based method	0.00044	0.00306

of the smooth ellipsoidal model is shown by a white arc, and the locations of the edges and normals are shown with red arrows. The white arc for the smooth body ellipse provides a clear visual reference for understanding the affect of terrain on edge localization. This is very clear in Fig. 26, where a mountain causes the horizon to depart slightly from the smooth body model.

Furthermore, both examples show a comparison between the new moment-based technique from Sec. IV.D.3 and the PAE method from [101]. Comparison is made with the PAE method because this was found to be the best performing method from the existing literature (see Table 2).

D. Example Optical Navigation Performance

The final example is a comparison of end-to-end OPNAV performance. In this analysis, a set of 342 synthetic images of the Moon was evaluated at distances of 13,000 to 229,000 km. In all cases, the OPNAV solution was found using the noniterative factorization method from Sec. II.B. Furthermore, performance results are presented for horizon localization with the PAE method from [101] and with the new moment-based algorithm presented in this paper.

The OPNAV performance for a smooth Moon is shown in Fig. 28, and the slight improvement offered by the new moment-based edge finding technique is evident. Likewise, the OPNAV performance for a Moon with an accurate terrain model is shown in Fig. 29. Because the improvement obtained from the new limb localization technique is difficult to quantitatively assess from these plots alone, the root-mean-square (RMS) errors are summarized in Table 3. RMS OPNAV errors are normalized by the distance to better compare results collected at different distances. These data again demonstrate that the new moment-based method outperforms the PAE method for OPNAV applications. They also demonstrate that the terrain (and not edge localization) can often dictate the achievable OPNAV performance.

VI. Conclusions

This paper provides a comprehensive treatment of image-based optical navigation (OPNAV) using only the lit limb of a planet or moon. New observations are made regarding the effect of local albedo

and terrain on OPNAV performance. Of particular note is a novel statistical model for describing terrain along a horizon arc. These observations led to the consideration of subpixel edge localization techniques for accurately finding the horizon's location in an image. In addressing this problem, a new moment-based technique for subpixel edge localization was developed and was found to substantially outperform 11 different existing methods. This new edge localization technique is put in the context of an end-to-end and noniterative OPNAV solution. The paper concludes with a number of practical examples. These examples show that iterative least-squares fitting of the horizon provides no additional performance improvement and that unmodeled terrain is often the driving error source.

Appendix A: Brief Historical Comment on the Lommel–Seeliger Law

What is known as the Lommel–Seeliger law today appears to have been developed by Lommel and Seeliger throughout the 1880s [47–50]. The earliest use of the term “Lommel–Seeliger law” that this author could find was by E. Anding in 1892, both in [104] and in his German translation of Lambert's *Photometria*. The name “Lommel–Seeliger law” appears to have been further popularized in Müller's 1897 book [105] and was in widespread use by the early 1900s. This naming convention continues into the modern literature. Despite all this, references to the early work of both Lommel and Seeliger are strangely lacking from most modern English works that reference the Lommel–Seeliger law. This brief comment aims to address this unfortunate shortcoming.

Appendix B: Equivalence of Edge Localization with Zernike Moments and Orthogonal Fourier–Mellin Moments

It was argued in Sec. IV.D.3 that there is no difference between subpixel edge localization with Zernike moments or with orthogonal Fourier–Mellin moments (OFMMs). Although this may be seen by comparing the numerical results in Table 2, it may also be shown analytically.

As the name might suggest, OFMMs use a circular Fourier transformation along with a radial Mellin transformation (a particular set of orthogonal radial polynomials) to construct moments in a polar coordinate system. Specifically, the OFMM is defined in polar coordinates as [102]

$$\Phi_{nm} = \frac{n+1}{\pi} \int_0^{2\pi} \int_0^1 f(r, \theta) V_{nm}(r, \theta) r dr d\theta \quad (\text{B1})$$

where $f(r, \theta)$ is the signal of which moments are desired, and $V_{nm}(r, \theta)$ are the OFMM kernel functions:

$$V_{nm}(r, \theta) = Q_n(r) \exp(jm\theta) \quad (\text{B2})$$

Note that the original OFMM work of [102] and the subsequent applications of this to edge detection [96–98] use $\exp(-jm\theta)$ instead of $\exp(jm\theta)$, but this distinction is not important. This only changes the sign convention for the angle θ . Thus, the same sign convention as in Sec. IV.D.3 is chosen to facilitate a direct comparison. The Mellin polynomials $Q_n(r)$ are defined as

$$Q_n(r) = \sum_{s=0}^n (-1)^{n+s} \left[\frac{(n+s+1)!}{(n-s)!s!(s+1)!} \right] r^s \quad (\text{B3})$$

which evaluate to

$$Q_0(r) = 1 \quad (\text{B4})$$

$$Q_1(r) = 3r - 2 \quad (\text{B5})$$

$$Q_2(r) = 10r^2 - 12r + 3 \quad (\text{B6})$$

\vdots

As with the Zernike moments, it is often convenient to define the integral term of OFMMs as ϕ_{nm}

$$\phi_{nm} = \int_0^{2\pi} \int_0^1 f(r, \theta) V_{nm}(r, \theta) r \, dr \, d\theta \quad (\text{B7})$$

such that

$$\Phi_{nm} = \frac{n+1}{\pi} \phi_{nm} \quad (\text{B8})$$

Now, it is evident that the four low-order Mellin polynomials may be related to the two Zernike polynomials used earlier. Specifically,

$$R_{11} = \frac{1}{3}(Q_1 + 2Q_0) = r \quad (\text{B9})$$

$$R_{20} = \frac{1}{5}(Q_2 + 4Q_1) = 2r^2 - 1 \quad (\text{B10})$$

which leads directly to the following equivalence between the Zernike kernel functions and OFMM kernel functions:

$$T_{11} = \frac{1}{3}(V_{11} + 2V_{01}) \quad (\text{B11})$$

$$T_{20} = \frac{1}{5}(V_{20} + 4V_{10}) \quad (\text{B12})$$

Furthermore, because integrals are linear operators, the corresponding moments follow the exact same relations:

$$A_{11} = \frac{1}{3}(\phi_{11} + 2\phi_{01}) \quad (\text{B13})$$

$$A_{20} = \frac{1}{5}(\phi_{20} + 4\phi_{10}) \quad (\text{B14})$$

Therefore, recalling Eq. (59), the edge location for the step function model is given by

$$l_s = \frac{A_{20}}{A_{11}} = \frac{3}{5} \left(\frac{\phi_{20} + 4\phi_{10}}{\phi_{11} + 2\phi_{01}} \right) \quad (\text{B15})$$

where the Zernike moment relation (center term) is the same as in [94], and the OFMM relation (rightmost term) is the same as in [96,97]. Thus, the edge location predicted by Zernike moments and OFMMs are analytically equivalent.

Appendix C: Notes on Analytic Integrals for Zernike Moments with Linear Ramp Edge Model

Recall that the definition of the Zernike moments is given by

$$A_{nm} = \iint_{\bar{u}^2 + \bar{v}^2 \leq 1} f(\bar{u}, \bar{v}) T_{nm}(\bar{u}, \bar{v}) \, d\bar{u} \, d\bar{v} \quad (\text{C1})$$

As discussed in Sec. IV.D.3, analytic integrals are computed in the frame aligned with the edge and described by the coordinates $\{\bar{u}', \bar{v}'\}$:

$$A'_{nm} = \iint_{\bar{u}'^2 + \bar{v}'^2 \leq 1} f(\bar{u}', \bar{v}') T_{nm}(\bar{u}', \bar{v}') \, d\bar{u}' \, d\bar{v}' \quad (\text{C2})$$

Substituting the piecewise linear ramp edge model of Eq. (42) for $f(\bar{u}', \bar{v}')$, the double integral in Eq. (C2) may be split into three regions as shown in Fig. C1 and described by

$$A'_{nm} = A'_{nm_1} + A'_{nm_2} + A'_{nm_3} \quad (\text{C3})$$

where

$$A'_{nm_1} = h \int_{-1}^1 \int_{-\sqrt{1-\bar{u}'^2}}^{\sqrt{1-\bar{u}'^2}} T_{nm}(\bar{u}', \bar{v}') \, d\bar{v}' \, d\bar{u}' \quad (\text{C4})$$

$$A'_{nm_2} = \frac{k}{2w} \int_{l_1}^{l_2} (\bar{u}' - l_1) \int_{-\sqrt{1-\bar{u}'^2}}^{\sqrt{1-\bar{u}'^2}} T_{nm}(\bar{u}', \bar{v}') \, d\bar{v}' \, d\bar{u}' \quad (\text{C5})$$

$$A'_{nm_3} = k \int_{l_2}^1 \int_{-\sqrt{1-\bar{u}'^2}}^{\sqrt{1-\bar{u}'^2}} T_{nm}(\bar{u}', \bar{v}') \, d\bar{v}' \, d\bar{u}' \quad (\text{C6})$$

Furthermore, the variables l_1 and l_2 describe the beginning and end of the edge ramp (see Fig. C2) and are defined as

$$l_1 = l - w \quad l_2 = l + w \quad (\text{C7})$$

C1. Derivation of A'_{11}

From Eq. (50), observe that $T_{11}(\bar{u}', \bar{v}') = \bar{u}' + j\bar{v}'$. All of the three contributing terms to A'_{11} share the same interior integral:

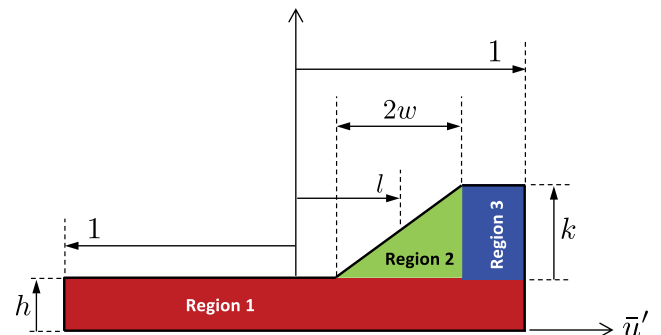


Fig. C1 Graphical depiction of the three regions used for computing integrals with the linear ramp edge model.

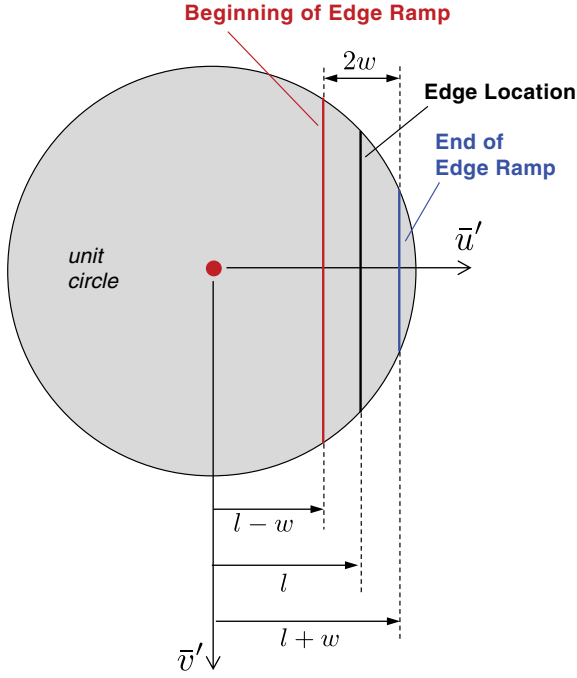


Fig. C2 Integration limits for computing A'_{nm} with the linear ramp edge model inside the unit circle.

$$\int_{-\sqrt{1-\bar{u}'^2}}^{\sqrt{1-\bar{u}'^2}} T_{11}(\bar{u}', \bar{v}') d\bar{v}' = \int_{-\sqrt{1-\bar{u}'^2}}^{\sqrt{1-\bar{u}'^2}} (\bar{u}' + j\bar{v}') d\bar{v}' = 2\bar{u}' \sqrt{1-\bar{u}'^2} \quad (\text{C8})$$

Therefore, consider the integral for A'_{11_1} :

$$A'_{11_1} = h \int_{-1}^1 \int_{-\sqrt{1-\bar{u}'^2}}^{\sqrt{1-\bar{u}'^2}} (\bar{u}' + j\bar{v}') d\bar{v}' d\bar{u}' \quad (\text{C9})$$

Substitute the result for the interior integral from Eq. (C8) such that the full integral for A'_{11_1} becomes

$$A'_{11_1} = 2h \int_{-1}^1 \bar{u}' \sqrt{1-\bar{u}'^2} d\bar{u}' = 0 \quad (\text{C10})$$

Now consider the integral for A'_{11_2} :

$$A'_{11_2} = \frac{k}{2w} \int_{l_1}^{l_2} (\bar{u}' - l_1) \int_{-\sqrt{1-\bar{u}'^2}}^{\sqrt{1-\bar{u}'^2}} (\bar{u}' + j\bar{v}') d\bar{v}' d\bar{u}' \quad (\text{C11})$$

Again, substitute the result for the interior integral from Eq. (C8) such that the full integral for A'_{11_2} becomes

$$\begin{aligned} A'_{11_2} &= \frac{k}{w} \int_{l_1}^{l_2} (\bar{u}' - l_1) \bar{u}' \sqrt{1-\bar{u}'^2} d\bar{u}' \\ &= \frac{k}{24w} \left\{ 3\sin^{-1}l_2 - 3\sin^{-1}l_1 - (5l_1 - 2l_1^3) \sqrt{1-l_1^2} \right. \\ &\quad \left. + (6l_2^3 - 3l_2) \sqrt{1-l_2^2} + 8l_1(1-l_2^2)^{3/2} \right\} \end{aligned} \quad (\text{C12})$$

Finally, consider the integral for A'_{11_3} :

$$A'_{11_3} = k \int_{l_2}^1 \int_{-\sqrt{1-\bar{u}'^2}}^{\sqrt{1-\bar{u}'^2}} (\bar{u}' + j\bar{v}') d\bar{v}' d\bar{u}' \quad (\text{C13})$$

Substitute the result for the interior integral from Eq. (C8) such that the full integral for A'_{11_3} becomes

$$A'_{11_3} = 2k \int_{l_2}^1 \bar{u}' \sqrt{1-\bar{u}'^2} d\bar{u}' = \frac{2k(1-l_2^2)^{3/2}}{3} \quad (\text{C14})$$

Therefore, substituting Eqs. (C10), (C12), and (C14) into Eq. (C3) and simplifying yields

$$\begin{aligned} A'_{11} &= \frac{k}{w} \int_{l_1}^{l_2} \bar{u}' (\bar{u}' - l_1) \sqrt{1-\bar{u}'^2} d\bar{u}' A'_{11} \\ &= \frac{k}{24w} \left\{ 3\sin^{-1}l_2 - 3\sin^{-1}l_1 - (5l_1 - 2l_1^3) \sqrt{1-l_1^2} \right. \\ &\quad \left. + (5l_2 - 2l_2^3) \sqrt{1-l_2^2} \right\} \end{aligned} \quad (\text{C15})$$

which is exactly the same as Eq. (61) presented in Sec. IV.D.3.

C2. Derivation of A'_{20}

From Eq. (51), observe that $T_{20}(\bar{u}', \bar{v}') = 2\bar{u}'^2 + 2\bar{v}'^2 - 1$. All of the three contributing terms to A'_{20} share the same interior integral:

$$\begin{aligned} \int_{-\sqrt{1-\bar{u}'^2}}^{\sqrt{1-\bar{u}'^2}} T_{20}(\bar{u}', \bar{v}') d\bar{v}' &= \int_{-\sqrt{1-\bar{u}'^2}}^{\sqrt{1-\bar{u}'^2}} (2\bar{u}'^2 + 2\bar{v}'^2 - 1) d\bar{v}' \\ &= \frac{2}{3} (4\bar{u}'^2 - 1) \sqrt{1-\bar{u}'^2} \end{aligned} \quad (\text{C16})$$

Therefore, consider the integral for A'_{20_1} :

$$A'_{20_1} = h \int_{-1}^1 \int_{-\sqrt{1-\bar{u}'^2}}^{\sqrt{1-\bar{u}'^2}} (2\bar{u}'^2 + 2\bar{v}'^2 - 1) d\bar{v}' d\bar{u}' \quad (\text{C17})$$

Substitute the result for the interior integral from Eq. (C16) such that the full integral for A'_{20_1} becomes

$$A'_{20_1} = \frac{2h}{3} \int_{-1}^1 (4\bar{u}'^2 - 1) \sqrt{1-\bar{u}'^2} d\bar{u}' = 0 \quad (\text{C18})$$

Now, consider the integral for A'_{20_2} :

$$A'_{20_2} = \frac{k}{2w} \int_{l_1}^{l_2} (\bar{u}' - l_1) \int_{-\sqrt{1-\bar{u}'^2}}^{\sqrt{1-\bar{u}'^2}} (2\bar{u}'^2 + 2\bar{v}'^2 - 1) d\bar{v}' d\bar{u}' \quad (\text{C19})$$

Again, substitute the result for the interior integral from Eq. (C16) such that the full integral for A'_{20_2} becomes

$$\begin{aligned} A'_{20_2} &= \frac{k}{3w} \int_{l_1}^{l_2} (\bar{u}' - l_1) (4\bar{u}'^2 - 1) \sqrt{1-\bar{u}'^2} d\bar{u}' \\ &= \frac{k}{15w} [(1-l_1^2)^{5/2} - (1-l_2^2)^{5/2}] - \frac{2kl_2(1-l_2^2)^{3/2}}{3} \end{aligned} \quad (\text{C20})$$

Finally, consider the integral for A'_{20_3} :

$$A'_{20_3} = k \int_{l_2}^1 \int_{-\sqrt{1-\bar{u}'^2}}^{\sqrt{1-\bar{u}'^2}} (2\bar{u}'^2 + 2\bar{v}'^2 - 1) d\bar{v}' d\bar{u}' \quad (\text{C21})$$

Substitute the result for the interior integral from Eq. (C16) such that the full integral for A'_{20_3} becomes

$$A'_{20_3} = \frac{2k}{3} \int_{l_2}^1 (4\bar{u}'^2 - 1) \sqrt{1-\bar{u}'^2} d\bar{u}' = \frac{2kl_2(1-l_2^2)^{3/2}}{3} \quad (\text{C22})$$

Therefore, substituting Eqs. (C18), (C20), and (C22) into Eq. (C3) and simplifying yields

$$A'_{20} = \frac{k}{15w} [(1 - l_1^2)^{5/2} - (1 - l_2^2)^{5/2}] \quad (C23)$$

which is exactly the same as Eq. (62) presented in Sec. IV.D.3.

Acknowledgments

This work was made possible by NASA under award NNX13AJ25A. The author thanks Chris D'Souza and Rebecca Johanning from NASA Johnson Space Center for encouragement to pursue this line of research; Andrew Liounis of the NASA Goddard Space Flight Center for feedback that led to the factorization presented in Sec. II.B.2; Bill Owen and Ed Riedel from NASA/California Institute of Technology Jet Propulsion Laboratory for insightful discussions about planetary atmospheres; Deborah Domingue from the Planetary Science Institute for help with Mercury images and photometric modeling; and Marian Armour-Gemmen and Barbara Hengemihle from the West Virginia University Library for help with finding the original sources for the Lommel–Seeliger law and for assistance in translating the original German.

References

- [1] Owen, W., Duxbury, T., Action, C., Synnott, S., Riedel, J., and Bhaskaran, S., "A Brief History of Optical Navigation at JPL," *Proceedings of the AAS Guidance and Control Conference*, American Astronautical Soc. Paper 08-053, Springfield, VA, Feb. 2008.
- [2] Owen, W., "Methods of Optical Navigation," *Proceedings of the AAS/AIAA Space Flight Mechanics Meeting*, American Astronautical Soc. Paper 11-215, Springfield, VA, Feb. 2011.
- [3] Thornton, C., and Border, J., *Radiometric Tracking Techniques for Deep Space Navigation*, Wiley, Hoboken, NJ, 2003, pp. 1–2.
- [4] Jerath, N., and Ohtakay, H., "Mariner IX Optical Navigation Using Mars Lit Limb," *Journal of Spacecraft and Rockets*, Vol. 11, No. 7, 1974, pp. 505–511.
doi:10.2514/3.62114
- [5] Campbell, J., Synnott, S., and Bierman, G., "Voyager Orbit Determination at Jupiter," *IEEE Transactions on Automatic Control*, Vol. 28, No. 3, 1983, pp. 256–268.
doi:10.1109/TAC.1983.1103223
- [6] Cheng, Y., Johnson, A., Matthies, L., and Olson, C., "Optical Landmark Detection for Spacecraft Navigation," *Proceedings of the AAS/AIAA Astrodynamics Specialist Conference*, American Astronautical Soc. Paper 02-224, Springfield, VA, Feb. 2003.
- [7] Gillam, S., Owen, W., Vaughan, A., Wang, T., Costello, J., Jacobson, R., Bluhm, D., Pojman, J., and Ionescu, R., "Optical Navigation for the Cassini/Huygens Mission," *Proceedings of the AAS/AIAA Astrodynamics Specialist Conference*, American Astronautical Soc. Paper 07-252, Springfield, VA, 2007.
- [8] Owen, W., Dumont, P., and Jackman, C., "Optical Navigation Preparations for New Horizons Pluto Flyby," *Proceedings of the 23rd International Symposium on Space Flight Dynamics (ISSFD)*, 2012.
- [9] Pimenta, F., "Astronomy and Navigation," *Handbook of Archaeoastronomy and Ethnoastronomy*, Springer-Verlag, New York, 2015, pp. 43–65.
- [10] Sobel, D., *Longitude*, Walker, New York, 1995, pp. 1–33.
- [11] Lampkin, B., "Sextant Sighting Performance for Space Navigation Using Simulated and Real Celestial Targets," *NAVIGATION: Journal of the Institute of Navigation*, Vol. 12, No. 4, 1965, pp. 312–320.
doi:10.1002/navi.1965.12.issue-4
- [12] Jorris, T., and Barth, A., "The USAF Manned Space Navigation Experiment on Apollo and Its Implications on Advanced Manned Spacecraft," *Proceedings of the Institute of Navigation National Space Meeting*, Inst. of Navigation, Washington, D.C., 1968, pp. 219–240.
- [13] Smith, D., and Lampkin, B., "Sextant Sighting Measurements from on Board the Gemini XII Spacecraft," NASA TN D-4952, Dec. 1968.
- [14] Draper, C., Wrigley, W., Hoag, D., Battin, R., Miller, J., Koso, D., Hopkins, A., and VanderVelde, W., "Space Navigation Guidance and Control, Vol. 1 of 2," NASA CR-75543, 1965.
- [15] Hoag, D., "The History of Apollo On-Board Guidance, Navigation, and Control," *Journal of Guidance, Control, and Dynamics*, Vol. 6, No. 1, 1983, pp. 4–13.
doi:10.2514/3.19795
- [16] Powers, S., "Preliminary Results from Skylab Experiment T002, Manual Navigation," *NAVIGATION: Journal of the Institute of Navigation*, Vol. 21, No. 4, 1974, pp. 279–287.
doi:10.1002/navi.1974.21.issue-4
- [17] Walsh, R., and Ferguson, J., "The United States Air Force Manual Space Navigation Experiment (DOD/NASA Skylab Experiment T-002)," *AIAA Astrodynamics Conference*, AIAA Paper 1976-0831, 1976.
- [18] Holt, G., "Crew-Aided Autonomous Navigation Project," NASA Johnson Space Center Rept. JSC-CN-33452, 2015.
- [19] Gioia, C., and Christian, J., "Gyro Bias Estimation Using Interior Star Angles for Manual Attitude Determination," *Journal of Spacecraft and Rockets*, Vol. 54, No. 2, 2017, pp. 513–522.
doi:10.2514/1.A33672
- [20] Duxbury, T., and Breckenridge, W., "Mariner Mars 1969 Optical Approach Navigation," *8th Aerospace Sciences Meeting*, AIAA Paper 1970-0070, 1970.
- [21] Synnott, S., Donegan, A., Riedel, J., and Stuve, J., "Interplanetary Optical Navigation: Voyager Uranus Encounter," *AIAA Astrodynamics Conference*, AIAA Paper 1986-2113, Aug. 1986.
- [22] Riedel, J., Owen, W., and Stuve, J., "Optical Navigation During the Voyager Neptune Encounter," *AIAA/AAS Astrodynamics Conference*, AIAA Paper 1990-2877, 1990.
- [23] Christian, J., "Optical Navigation for a Spacecraft in a Planetary System," Ph.D. Dissertation, Univ. of Texas at Austin, Austin, TX, 2010.
- [24] Christian, J., and Lightsey, E., "Onboard Image-Processing Algorithm for a Spacecraft Optical Navigation Sensors System," *Journal of Guidance, Control, and Dynamics*, Vol. 49, No. 2, 2012, pp. 337–352.
doi:10.2514/1.A32065
- [25] Li, S., Lu, R., Zhang, L., and Peng, Y., "Image Processing Algorithms for Deep-Space Autonomous Optical Navigation," *Journal of Navigation*, Vol. 66, No. 4, 2013, pp. 605–623.
doi:10.1017/S0373463313000131
- [26] Christian, J., "Optical Navigation Using Planet's Centroid and Apparent Diameter in Image," *Journal of Guidance, Control, and Dynamics*, Vol. 38, No. 2, 2015, pp. 192–204.
doi:10.2514/1.G000872
- [27] Mortari, D., de Dilectis, F., and Zanetti, R., "Position Estimation Using the Image Derivative," *Aerospace*, Vol. 2, No. 3, 2015, pp. 435–460.
doi:10.3390/aerospace2030435
- [28] Christian, J., "Optical Navigation Using Iterative Horizon Reprojection," *Journal of Guidance, Control, and Dynamics*, Vol. 39, No. 5, 2016, pp. 1092–1103.
doi:10.2514/1.G001569
- [29] Christian, J., and Robinson, S., "Non-Iterative Horizon-Based Optical Navigation by Cholesky Factorization," *Journal of Guidance, Control, and Dynamics*, Vol. 39, No. 12, 2016, pp. 2757–2765.
doi:10.2514/1.G000539
- [30] Hikes, J., Liounis, A., and Christian, J., "Parametric Covariance Model for Horizon-Based Optical Navigation," *Journal of Guidance, Control, and Dynamics*, Vol. 40, No. 1, 2017, pp. 170–178.
doi:10.2514/1.G000708
- [31] Du, S., Wang, M., Chen, X., Fang, S., and Su, H., "A High-Accuracy Extraction Algorithm of Planet Centroid Image in Deep-Space Autonomous Optical Navigation," *Journal of Navigation*, Vol. 69, No. 4, 2016, pp. 828–844.
doi:10.1017/S0373463315000910
- [32] Mortari, D., D'Souza, C., and Zanetti, R., "Image Processing of Illuminated Ellipsoid," *Journal of Spacecraft and Rockets*, Vol. 53, No. 3, 2016, pp. 448–456.
doi:10.2514/1.A33342
- [33] Bu, Y., Zhang, Q., Ding, C., Tang, G., Wang, H., Qiu, R., Liang, L., and Yin, H., "A Novel Interplanetary Optical Navigation Algorithm Based on Earth? Moon Group Photos by Chang'e-5T1 Probe," *Advances in Space Research*, Vol. 59, No. 3, Feb. 2017, pp. 907–915.
doi:10.1016/j.asr.2016.07.004
- [34] Goodman, J. L., "Apollo 13 Guidance, Navigation, and Control Challenges," *AIAA SPACE 2009 Conference and Exposition*, AIAA Paper 2009-6455, Sept. 2009.
- [35] Christian, J., Benhacine, L., Hikes, J., and D'Souza, C., "Geometric Calibration of the Orion Optical Navigation Camera Using Star Field Images," *Journal of the Astronautical Sciences*, Vol. 63, No. 4, 2016, pp. 335–353.
doi:10.1007/s40295-016-0091-3
- [36] Ma, Y., Soatto, S., Košecák, J., and Sastry, S., *An Invitation to 3-D Vision: From Images to Geometric Models*, Springer, New York, 2010, pp. 49–59.

- [37] Golub, G., and Van Loan, C., *Matrix Computations*, 4th ed., Johns Hopkins Univ. Press, Baltimore, MD, 2013, pp. 76–80, 163–165.
- [38] Hansen, J., and Travis, L., “Light Scattering in Planetary Atmospheres,” *Space Science Reviews*, Vol. 16, No. 4, 1974, pp. 527–610.
doi:10.1007/BF00168069
- [39] McCartney, E., *Optics of the Atmosphere: Scattering by Molecules and Particles*, Wiley, New York, 1976, pp. 1–49.
- [40] Rayleigh, L. (Strutt, J. W.), “On the Light from the Sky, Its Polarization and Colour,” *Philosophical Magazine Series 4*, Vol. 41, No. 271, 1871, pp. 107–120.
- [41] Mie, G., “Beiträge zur Optik Trüber Medien, Speziell Kolloidaler Metallösungen,” *Annalen der Physik*, Vol. 330, No. 3, 1908, pp. 377–445.
doi:10.1002/(ISSN)1521-3889
- [42] Nishita, T., Sirai, T., Tadamura, K., and Nakamae, E., “Display of the Earth Taking into Account Atmospheric Scattering,” *Proceedings of the 20th Annual Conference on Computer Graphics and Interactive Techniques (SIGGRAPH '93)*, 1993, pp. 175–182.
doi:10.1145/166117.166140
- [43] Sloup, J., “A Survey of the Modeling and Rendering of the Earth’s Atmosphere,” *Proceedings of the 18th Spring Conference on Computer Graphics (SCCG '02)*, 2002, pp. 141–150.
doi:10.1145/584458.584482
- [44] Bruneton, E., and Neyret, F., “Precomputed Atmospheric Scattering,” *Proceedings of the Eurographics Symposium on Rendering*, 2008, pp. 1079–1086.
doi:10.1111/j.1467-8659.2008.01245.x
- [45] Christian, J., “Horizon-Based Optical Navigation Using Images of a Planet with an Atmosphere,” *AIAA/AAS Astrodynamics Specialist Conference*, AIAA Paper 2016-5442, 2016.
- [46] Lambert, J., *Photometria*, 1760.
- [47] Lommel, E., “Ueber Fluorescenz,” *Annalen der Physik*, Vol. 246, No. 7, 1880, pp. 449–472.
doi:10.1002/(ISSN)1521-3889
- [48] Seeliger, H., “Bemerkungen zu Zöllner’s ‘Photometrischen Untersuchungen’,” *Vierteljahrshfte der Astronomischen Gesellschaft*, Vol. 21, 1886, pp. 216–229.
- [49] Lommel, E., “Sitzungsberichte der Mathematisch-Physikalischen,” *Annalen der Physik*, Vol. 17, 1887, pp. 95–132.
- [50] Seeliger, H., “Zur Photometrie Zerstreut Reflectirender Substanzen,” *Sitzungsberichte der Mathematisch-Physikalischen Classe der K.B. Akademie der Wissenschaften zu Munchen*, Vol. 18, 1888, pp. 201–248.
- [51] Hapke, B., “A Theoretical Photometric Function for the Lunar Surface,” *Journal of Geophysical Research*, Vol. 68, No. 15, 1963, pp. 4571–4586.
doi:10.1029/JZ068i015p04571
- [52] Hapke, B., “Bidirectional Reflectance Spectroscopy 1. Theory,” *Journal of Geophysical Research*, Vol. 86, No. B4, 1981, pp. 3039–3054.
doi:10.1029/JB086iB04p03039
- [53] Fairbairn, M., “Planetary Photometry: The Lommel–Seeliger Law,” *Journal of the Royal Astronomical Society of Canada*, Vol. 99, No. 3, 2005, pp. 92–93.
- [54] Kasseinen, M., Torppa, J., and Muinonen, K., “Optimization Methods for Asteroid Lightcurve Inversion: 2. The Complete Inverse Problem,” *Icarus*, Vol. 153, No. 1, 2001, pp. 37–51.
doi:10.1006/icar.2001.6674
- [55] Shkuratov, Y., Kaydash, V., Korokhin, V., Velikodsky, Y., Opanasenko, N., and Videen, G., “Optical Measurements of the Moon as a Tool to Study Its Surface,” *Planetary and Space Science*, Vol. 59, No. 13, 2011, pp. 1326–1371.
doi:10.1016/j.pss.2011.06.011
- [56] Domingue, D., Denevi, B., Murchie, S., and Hash, C., “Application of Multiple Photometric Models to Disk-Resolved Measurements of Mercury’s Surface: Insights into Mercury’s Regolith Characteristics,” *Icarus*, Vol. 268, 2016, pp. 172–203.
doi:10.1016/j.icarus.2015.11.040
- [57] Schröder, S., Mottola, S., Keller, H., Raymond, C., and Russell, C., “Resolved Photometry of Vesta Reveals Physical Properties of Crater Regolith,” *Planetary and Space Science*, Vol. 85, 2013, pp. 198–213.
doi:10.1016/j.pss.2013.06.009
- [58] Buratti, B., and Veeverka, J., “Voyager Photometry of Europa,” *Icarus*, Vol. 55, No. 1, 1983, pp. 93–110.
doi:10.1016/0019-1035(83)90053-2
- [59] McEwen, A., “Exogenic and Endogenic Albedo and Color Patterns for Europa,” *Journal of Geophysical Research*, Vol. 91, No. B8, 1986, pp. 8077–8097.
doi:10.1029/JB091iB08p08077
- [60] McEwen, A., “Photometric Functions for Photoclinometry and Other Applications,” *Icarus*, Vol. 92, No. 2, 1991, pp. 298–311.
doi:10.1016/0019-1035(91)90053-V
- [61] Hapke, B., “Bidirectional Reflectance Spectroscopy 3. Corrections for Macroscopic Roughness,” *Icarus*, Vol. 59, No. 1, 1984, pp. 41–59.
doi:10.1016/0019-1035(84)90054-X
- [62] Hapke, B., “Bidirectional Reflectance Spectroscopy 4. The Extinction Coefficient and the Opposition Effect,” *Icarus*, Vol. 67, No. 2, 1986, pp. 264–280.
doi:10.1016/0019-1035(86)90108-9
- [63] Hapke, B., “Bidirectional Reflectance Spectroscopy 5. The Coherent Backscatter Opposition Effect and Anisotropic Scattering,” *Icarus*, Vol. 157, No. 2, 2002, pp. 523–534.
doi:10.1006/icar.2002.6853
- [64] Hapke, B., “Bidirectional Reflectance Spectroscopy 6. Effects of Porosity,” *Icarus*, Vol. 195, No. 2, 2008, pp. 918–926.
doi:10.1016/j.icarus.2008.01.003
- [65] Hapke, B., “Bidirectional Reflectance Spectroscopy 7. The Single Particle Phase Function Hockey Stick Relation,” *Icarus*, Vol. 221, No. 2, 2012, pp. 1079–1083.
doi:10.1016/j.icarus.2012.10.022
- [66] Hapke, B., *Theory of Reflectance and Emittance Spectroscopy*, 2nd ed., Cambridge Univ. Press, Cambridge, England, U.K., 2012, pp. 180–220, 303–338.
- [67] Sato, H., Robinson, M., Hapke, B., Denevi, B., and Boyd, A., “Resolved Hapke Parameter Maps of the Moon,” *Journal of Geophysical Research: Planets*, Vol. 119, 2014, pp. 1775–1805.
doi:10.1002/2013JE004580
- [68] Porco, C., “Cassini Orbiter Earth/Venus/Jupiter ISSNA/ISSWA 2 EDR V1.0, CO-E/V/J-ISSNA/ISSWA-2-EDR-V1.0,” NASA Planetary Data System, 2008.
- [69] Hash, C., “Messenger MDIS Experiment (EDR) Data E/V/H V1.0,” NASA Planetary Data System, 2008.
- [70] Zuber, M. T., et al., “Topography of the Northern Hemisphere of Mercury from MESSENGER Laser Altimetry,” *Science*, Vol. 336, No. 6078, 2012, pp. 217–220.
doi:10.1126/science.1218805
- [71] Smith, D. E., et al., “Initial Observations from the Lunar Orbiter Laser Altimeter (LOLA),” *Geophysical Research Letters*, Vol. 37, No. 18, 2010.
doi:10.1029/2010GL043751
- [72] Smith, D. E., et al., “Mars Orbiter Laser Altimeter: Experiment Summary After the First Year of Global Mapping of Mars,” *Journal of Geophysical Research*, Vol. 106, No. E10, 2001, pp. 23,689–23,722.
doi:10.1029/2000JE001364
- [73] Smith, D. E., et al., “The Lunar Orbiter Laser Altimeter Investigation on the Lunar Reconnaissance Orbiter Mission,” *Space Science Reviews*, Vol. 150, No. 1, 2010, pp. 209–241.
doi:10.1007/s11214-009-9512-y
- [74] Chin, G., et al., “Lunar Reconnaissance Orbiter Overview: The Instrument Suite and Mission,” *Space Science Reviews*, Vol. 129, No. 4, 2007, pp. 391–419.
doi:10.1007/s11214-007-9153-y
- [75] Neumann, G., “Lunar Orbiter Laser Altimeter Raw Data Set, LRO-L-LOLA-4-GDR-V1.0,” NASA Planetary Data System, 2009.
- [76] Gelb, A., *Applied Optimal Estimation*, MIT Press, Cambridge, MA, 1974, pp. 81–82.
- [77] Brown, D., “Decentering Distortion of Lenses,” *Photogrammetric Engineering*, Vol. 32, No. 3, 1966, pp. 444–462.
- [78] Brown, D., “Close-Range Camera Calibration,” *Photogrammetric Engineering*, Vol. 37, No. 8, 1971, pp. 522–566.
- [79] Folkner, W., Williams, J., Boggs, D., Park, R., and Kuchynka, P., “The Planetary and Lunar Ephemerides DE430 and DE431,” The Interplanetary Network Progress Rept. 42-196, 2014, <http://ipnpr.jpl.nasa.gov>.
- [80] Jones, R., “On the Point and Line Spread Functions of Photographic Images,” *Journal of the Optical Society of America*, Vol. 48, No. 12, 1958, pp. 934–937.
doi:10.1364/JOSA.48.000934
- [81] Gopala Rao, U., and Jain, V., “Gaussian and Exponential Approximations of the Modulation Transfer Function,” *Journal of the Optical Society of America*, Vol. 57, No. 9, 1967, pp. 1159–1160.
doi:10.1364/JOSA.57.001159
- [82] Forsyth, D., and Ponce, J., *Computer Vision: A Modern Approach*, Prentice-Hall, Upper Saddle River, NJ, 2003, pp. 165–187.

- [83] Gonzales, R., and Woods, R., *Digital Image Processing*, 3rd ed., Prentice-Hall, Upper Saddle River, NJ, 2008, pp. 706–728.
- [84] Roberts, L., “Machine Perception of Three-Dimensional Solids,” *Optical and Electro-Optical Information Processing*, edited by Tippet, J., MIT Press, Cambridge, MA, 1965, pp. 159–197.
- [85] Prewitt, J., “Object Enhancement and Extraction,” *Picture Processing and Psychopictorics*, edited by Lipkin, B., and Rosenfeld, A., Academic Press, New York, 1970, pp. 75–150.
- [86] Duda, R., and Hart, P., *Pattern Classification and Scene Analysis*, Wiley, New York, 1973, pp. 271–272.
- [87] Marr, D., and Hildreth, E., “Theory of Edge Detection,” *Proceedings of the Royal Society of London B*, Vol. 207, No. 1167, 1980, pp. 187–217. doi:10.1098/rspb.1980.0020
- [88] Canny, J., “A Computational Approach to Edge Detection,” *IEEE Transactions on Pattern Analysis and Machine Intelligence*, Vol. 8, No. 6, 1986, pp. 679–698. doi:10.1109/TPAMI.1986.4767851
- [89] Kovese, P., “Phase Congruency: A Low-Level Image Invariant,” *Psychological Research*, Vol. 64, No. 2, 2000, pp. 136–148. doi:10.1007/s004260000024
- [90] Kovese, P., “Phase Congruency Detects Corners and Edges,” *Proceedings of the Australian Pattern Recognition Society Conference: DICTA 2003*, 2003.
- [91] Tabatabai, A., and Mitchell, O., “Edge Location to Subpixel Values in Digital Imagery,” *IEEE Transactions on Pattern Analysis and Machine Intelligence*, Vol. 6, No. 2, 1984, pp. 188–201. doi:10.1109/TPAMI.1984.4767502
- [92] Jensen, K., and Anastassiou, D., “Subpixel Edge Localization and the Interpolation of Still Images,” *IEEE Transactions on Image Processing*, Vol. 4, No. 3, 1995, pp. 285–295. doi:10.1109/83.366477
- [93] Lyvers, E., Mitchell, O., Akey, M., and Reeves, A., “Subpixel Measurements Using a Moment-Based Edge Operator,” *IEEE Transactions on Pattern Analysis and Machine Intelligence*, Vol. 11, No. 12, 1989, pp. 1293–1309. doi:10.1109/34.41367
- [94] Ghosal, S., and Mehrotra, R., “Orthogonal Moment Operators for Subpixel Edge Detection,” *Pattern Recognition*, Vol. 26, No. 2, 1993, pp. 295–306. doi:10.1016/0031-3203(93)90038-X
- [95] Ying-Dong, Q., Cheng-Sing, C., San-Ben, C., and Jin-Quan, L., “A Fast Subpixel Edge Detection Method Using Sobel–Zernike Moments Operator,” *Image and Vision Computing*, Vol. 23, No. 1, 2005, pp. 11–17. doi:10.1016/j.imavis.2004.07.003
- [96] Tan, J., Ao, L., Cui, J., and Kang, W., “Further Improvement of Edge Location Accuracy of Charge-Coupled-Device Laser Autocollimators Using Orthogonal Fourier–Mellin Moments,” *Optical Engineering*, Vol. 46, No. 5, 2007, Paper 057007. doi:10.1117/1.2735287
- [97] Bin, T., Lei, A., Jiwen, C., Wenjing, K., and Dandan, L., “Subpixel Edge Location Based on Orthogonal Fourier–Mellin Moments,” *Image and Vision Computing*, Vol. 26, No. 4, 2008, pp. 563–569. doi:10.1016/j.imavis.2007.07.003
- [98] Da, F., and Zhang, H., “Sub-Pixel Edge Detection Based on an Improved Moment,” *Image and Vision Computing*, Vol. 28, No. 12, 2010, pp. 1645–1658. doi:10.1016/j.imavis.2010.05.003
- [99] Ye, J., Fu, G., and Poudel, U., “High-Accuracy Edge Detection with Blurred Edge Model,” *Image and Vision Computing*, Vol. 23, No. 5, 2005, pp. 453–467. doi:10.1016/j.imavis.2004.07.007
- [100] Hermosilla, T., Bermejo, E., Balaguer, A., and Ruiz, L., “Non-Linear Fourth-Order Image Interpolation for Subpixel Edge Detection and Localization,” *Image and Vision Computing*, Vol. 26, No. 9, 2008, pp. 1240–1248. doi:10.1016/j.imavis.2008.02.012
- [101] Trujillo-Pino, A., Krissian, K., Aleman-Flores, M., and Santana-Cedres, D., “Accurate Subpixel Edge Location Based on Partial Area Effect,” *Image and Vision Computing*, Vol. 31, No. 1, 2013, pp. 72–90. doi:10.1016/j.imavis.2012.10.005
- [102] Sheng, Y., and Shen, L., “Orthogonal Fourier–Mellin Moments for Invariant Pattern Recognition,” *Journal of the Optical Society of America*, Vol. 11, No. 6, 1994, pp. 1748–1757. doi:10.1364/JOSAA.11.001748
- [103] Fischler, M., and Bolles, R., “Random Sample Consensus: A Paradigm for Model Fitting with Applications to Image Analysis and Automated Cartography,” *Communications of the ACM*, Vol. 24, No. 6, 1981, pp. 381–395. doi:10.1145/358669.358692
- [104] Anding, E., “Ueber die Lichtvertheilung auf einer Unvollständig Beleuchteten Planetenscheibe,” *Astronomische Nachrichten*, Vol. 129, No. 25, 1892, pp. 377–388. doi:10.1002/(ISSN)1521-3994
- [105] Müller, G., *Die Photometrie der Gestirne*, Engelmann, Leipzig, Germany, 1897, pp. 56–109.

D. A. Spencer
Associate Editor